Chapter 9
Lasing in Amorphous Nanophotonic Structures

Hui Cao and Heeso Noh

Abstract We review the recent experimental and numerical studies on lasing in photonic nanostructures with short-range order in this chapter. Despite the lack of long-range order, photonic bandgaps can be formed in such structures, and they are isotropic. Our numerical studies show that the photonic bandgaps depends not only on the spatial range of geometric order, but also on the structural topology. The photonic bandedge modes may be spatially localized, in contrast to those of photonic crystals. Lasing has been realized experimentally in semiconductor nanostructures with short-range order. The nature of lasing modes are illustrated, and the lasing characteristic can be controlled by the short-range order.

9.1 Introduction

Over the past decade lasing has been realized in various types of nanostructures. The most common one is the photonic crystal (PhC) with periodic modulation of the refractive index that result in the formation of photonic bandgap (PBG) [1]. The distributed feedback PhC laser relies on the slow group velocity at a photonic bandedge to enhance light amplification [2]. The PhC defect mode laser utilizes light localization at a structural defect to minimize the lasing threshold [3, 4]. In addition to PhCs, lasing action in photonic quasi-crystals with and without defects has been reported [5–9]. Despite lack of periodicity, the quasi-crystalline photonic structure has long-range orientational order and can possess a PBG.

The photonic amorphous structure (PAS) has neither long-range translational order nor orientational order. However, the density of optical states (DOS) may be depleted through coupled Mie resonances [10–15] or short-range structural order [16, 17]. PBGs also exist in amorphous photonic structures that consist of

H. Cao (✉)
Department of Applied Physics, Yale University, New Haven, CT 06520, USA
e-mail: hui.cao@yale.edu

H. Noh
Department of Nano and Electronic Physics, Kookmin University, Seoul, Korea
e-mail: heesonoh@kookmin.ac.kr

C. Rockstuhl, T. Scharf (eds.), *Amorphous Nanophotonics*,
Nano-Optics and Nanophotonics, DOI 10.1007/978-3-642-32475-8_9,

strong Mie scatterers such as dielectric rods or spheres [10–14]. These structures are termed photonic glasses [15], in analogy to glassy silica, which has an electronic band gap spanning the entire visible frequency range. In the absence of Mie resonance, Bragg scattering of propagating waves by local domains can produce PBGs in structures with only short-range positional order. For example, complete PBGs exist in photonic amorphous diamond structures—three-dimensional (3D) continuous random networks with diamond-like tetrahedral-bonding between particles [16]. Recently hyper-uniform disordered materials with short-range geometric order and uniform local topology have been shown to posses large PBGs [17]. Unique optical features of amorphous media have also been investigated experimentally [18].

Despite these studies, little is known about the transition from PhCs to amorphous optical materials, e.g., how does the density of optical states (DOS) evolve as the structural properties of the material change from ordered to amorphous? Is there a critical size of ordered domains in polycrystalline materials below which the system becomes optically amorphous? Our recent work aimed to answer the above questions by mapping out the transition from photonic polycrystalline to amorphous structures [19]. Moreover, we have performed systematic study on lasing characteristic in polycrystalline and amorphous structures [20, 21]. It reveals what determines the lasing frequencies as well as the nature of lasing modes. These studies provide a physical insight to lasing mechanism in photonic structures lacking long-range order.

In fact, nature utilizes both crystalline and amorphous photonic structures for color generation [22–25]. Periodic structures are intrinsically anisotropic, thus the colors they produce are iridescent (i.e., change with viewing angle). In photonic polycrystals, the cumulative effect of a large number of randomly orientated crystallites makes the color non-iridescent [26]. Photonic amorphous media can also produce vivid non-iridescent colors via short-range structural order [27]. Although the refractive index contrast is usually too low to form PBGs in most biological systems, the interference of scattered light selects the color whose wavelength corresponds to the structural correlation length [28]. Therefore, short-range positional order can significantly modify photonic properties [29–31], leading to unique applications [32]. Lately we have utilized the short-range order to enhance optical confinement and improve the lasing efficiency in PAS.

9.2 Photonic Polycrystals and Amorphous Structures

9.2.1 Photonic Bandgap Effects and Enhanced Light Confinement

We start with the numerical study on PBGs and high-quality (Q) modes in two-dimensional (2D) photonic structures with short-range positional order.

Structure Generation and Characterization

To create 2D photonic polycrystals and amorphous structures, we have developed numerical simulation methods to generate N cylinders of circular shape in a square

box with periodic boundaries. For the purpose of generating configurations with varying positional order, we assume that the cylinders interact elastically via the purely repulsive short-range linear spring potential

$$V(r_{ij}) = \frac{b}{2}\left(1 - \frac{r_{ij}}{d_{ij}}\right)^2 \theta\left(1 - \frac{r_{ij}}{d_{ij}}\right), \tag{9.1}$$

where r_{ij} is the center-to-center distance between cylinders i and j, b is the characteristic energy scale of the interaction, $\theta(x)$ is the Heaviside function, and $d_{ij} = (d_i + d_j)/2$ is the average diameter of cylinders i and j. To vary the degree of positional order, the cylinders are polydisperse—with a uniform distribution of diameters between d_0 and $d_0(1 + p)$, where p is the polydispersity that ranges from 0 to 0.5. The average diameter $\langle d \rangle = d_0(1 + p/2)$.

Initially d_0, or the packing fraction

$$\phi = \left(\frac{1}{L}\right)^2 \sum_{i=1}^{N} \pi \left(\frac{d_i}{2}\right)^2, \tag{9.2}$$

is set to a small value $\phi_0 = 0.2$, and we place N cylinders randomly within a square of side length L. We then gradually increase the diameters of all cylinders while maintaining the relative size distribution to create a jammed packing of cylinders [33]. Each increment in diameter is followed by minimization of the total potential energy $V = \sum_{i>j} V(r_{ij})$ of the system. The energy minimization process is similar to moving each cylinder along the direction of the total force on it using overdamped dynamics. When V drops below a threshold value or the difference in energy between successive minimization steps is less than a small tolerance, the minimization process is terminated. If V is zero and gaps exist between cylinders, the system is unjammed, and it is compressed with a further increase of d_0. If $V > 0$ after the energy minimization process, a large system-spanning number of cylinders are overlapped. To eliminate overlap, the system is decompressed, i.e., d_0 is uniformly decreased for all cylinders. The energy minimization process is repeated after the decompression step to find the local potential energy minimum. If $V = 0$, the system is compressed; if not, the system is decompressed again. The increment by which the packing fraction of the cylinders is changed at each compression or decompression step is gradually reduced to zero. Eventually when all of the cylinders are just touching and the net force on each cylinder is nearly zero, the system is considered "jammed", and the process to increase the packing fraction is stopped.

For each polydispersity p, we generated at least 100 static, jammed packings of cylinders from random initial configurations. The values of ϕ are typically in the range between 0.82 and 0.85 with varying degrees of positional order. After generating jammed packings, we reduce the diameters of all cylinders to the same value D (with $\phi = 0.5$) to eliminate the size polydispersity. Thus, in the final configurations, the *structural disorder* exists only in the positions of the cylinders with order decreasing monotonically with increasing p. Figure 9.1 (a) shows the typical configurations of $N = 1024$ cylinders generated with $p = 0.1$ (left), 0.3 (middle),

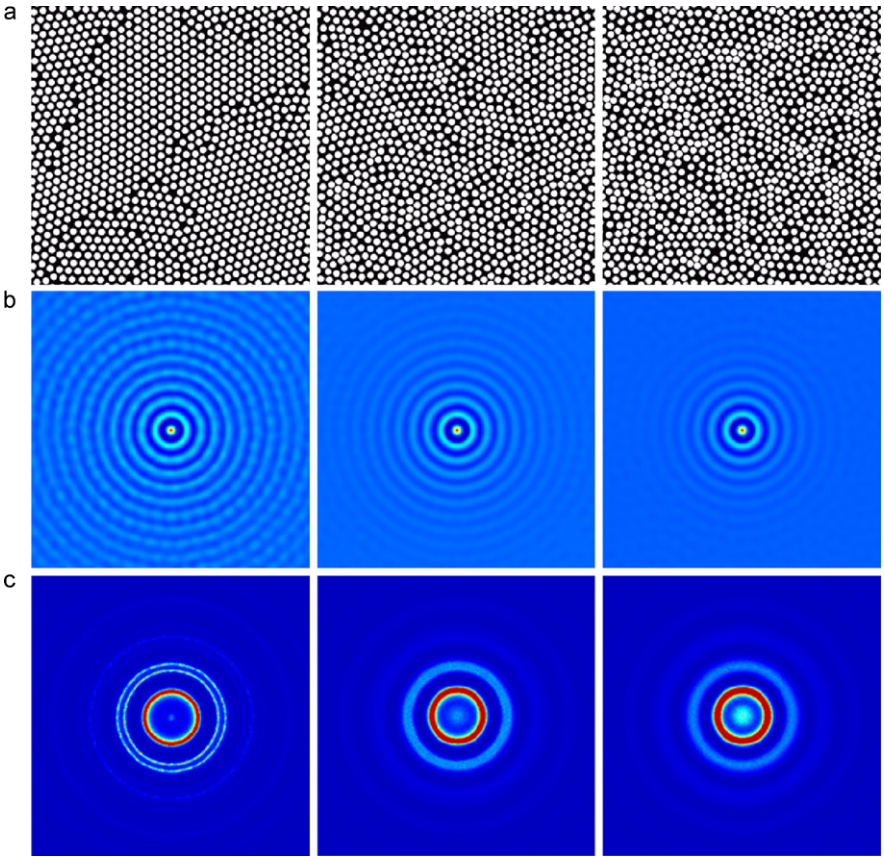

Fig. 9.1 (**a**) Typical configurations of two-dimensional arrays of air cylinders (*white*) in a dielectric host (*black*), generated using Protocol 9.1 described in Sect. 9.2.1 with polydispersity $p = 0.1$ (*left*), 0.3 (*middle*), and 0.5 (*right*). (**b**) Contour plot of the ensemble-averaged density spatial autocorrelation function $C(\Delta \boldsymbol{r})$ and (**c**) Power spectra $|f(\boldsymbol{q})|^2$ from Fourier transformed density for the same polydispersities in (**a**). The *scale bars* in (**b**) and (**c**) are $5D$ and $1/D$, where D is the diameter of cylinders in (**a**). Reprinted with permission from [19], Copyright 2008, Wiley-VCH

and 0.5 (right). For $p = 0.1$, the system contains several domains of cylinders with crystalline order, but each possesses a different orientation. With increasing p, the domains have reduced positional order and decrease in size.

To quantify the structural order, we calculate the ensemble-averaged spatial correlation function of the density, the Fourier transform of the density, the radial distribution function $g(r)$, and the local and global bond orientational order parameters. The spatial autocorrelation function of density $\rho(\mathbf{r}) = L^{-2} \sum_{i=1}^{N} \theta(\mathbf{r} - \mathbf{r}_i)$ is given by

$$C(\Delta \mathbf{r}) = \frac{\langle \rho(\mathbf{r}) \rho(\mathbf{r} + \Delta \mathbf{r}) \rangle - \langle \rho(\mathbf{r}) \rangle^2}{\langle \rho(\mathbf{r}) \rangle^2}. \tag{9.3}$$

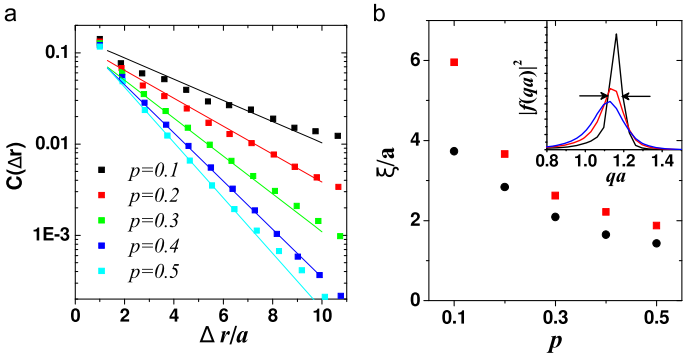

Fig. 9.2 (**a**) Logarithmic plot of the peak amplitudes for the ensemble- and angle-averaged density spatial autocorrelation function $C(\Delta\mathbf{r})$ for $p = 0.1$, 0.2, 0.3, 0.4, and 0.5. $a = L/N^{1/2}$ is the average distance between adjacent cylinders. The exponential fits of the data (*solid lines*) give the decay length ξ_r. (**b**) *Inset*: The first peaks of the angle- and ensemble-averaged Fourier transformed density $|f(qa)|^2$ for $p = 0.1$ (*solid line*), 0.2 (*dashed line*), and 0.4 (*short-dashed line*), whose width gives the average domain size ξ_q. *Main panel*: ξ_r (*circles*) and ξ_q (*squares*) versus p. Reprinted with permission from [19], Copyright 2008, Wiley-VCH

$C(\Delta\mathbf{r})$ is averaged first over the spatial coordinates of the cylinders $\mathbf{r}$ within one configuration, and then over at least 100 independent configurations. A contour plot of $C(\Delta\mathbf{r})$ is displayed in Fig. 9.1 (b) as a function of increasing p (from left to right) used to generate the configurations. For $p = 0.1$, $C(\Delta\mathbf{r})$ displays a large number of concentric rings and a modulation of the amplitude within a given ring, which indicates strong positional order. As p increases the system becomes more disordered and isotropic, since the number of visible concentric rings decreases and the amplitude within a given ring becomes more uniform. After integrating $C(\Delta\mathbf{r})$ over the polar angle, we plot in Fig. 9.2 (a) the peak amplitudes of the rings as a function of $\Delta r/a$, where $a = L/N^{1/2}$ is the average center-to-center distance between neighboring cylinders. The peak amplitudes decay more rapidly with Δr at larger p. The decay is approximately exponential, if we exclude the first peak near $\Delta r = a$. The faster decay from the first peak to the second arises from correlations induced by the just-touching jammed cylinders. The decay length ξ_r is extracted from the exponential fit $\exp[-\Delta r/\xi_r]$ of peak amplitudes after excluding the first peak. As shown in Fig. 9.2 (b), ξ_r is smaller for larger p, indicating the range of spatial order becomes shorter.

We also calculated the spatial Fourier transform of the structures, $f(\mathbf{q}) = \int d^2\mathbf{r} \exp[-i\mathbf{q}\cdot\mathbf{r}]\rho(\mathbf{r})$, where $\mathbf{q}$ is the wavevector. Figure 9.1 (c) displays the ensemble-averaged power spectra $|f(\mathbf{q})|^2$ for $p = 0.1$, 0.3 and 0.5, which consist of concentric rings. The radial width of the rings increases with p, as can be seen clearly for the first ring (with the smallest radius). The second and third rings are distinct for $p = 0.1$, which indicates the six-fold symmetry of the cylinders within each domain. For $p = 0.3$ and 0.5, these rings become wider and merge together. We integrate $|f(\mathbf{q})|^2$ over all directions of $\mathbf{q}$ to obtain the intensity as a function of the amplitude q. The inset of Fig. 9.2 (b) displays the intensity of the first ring versus

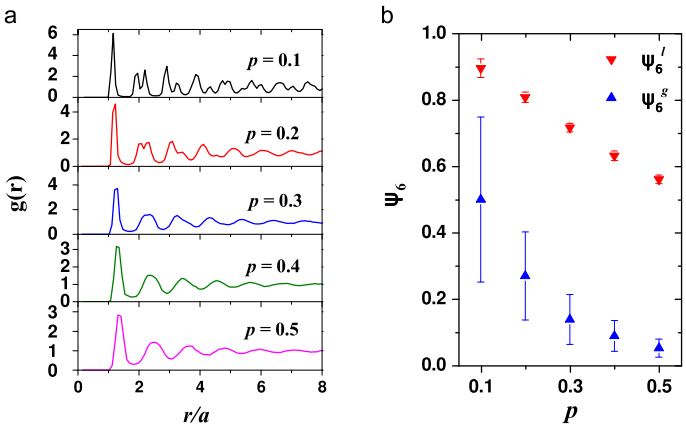

Fig. 9.3 (**a**) Radial distribution function $g(r)$ for $p = 0.1$, 0.2, 0.3, 0.4, and 0.5. (**b**) Local ψ_6^l (*downward triangles*) and global ψ_6^g (*upward triangles*) bond-orientational order parameters versus polydispersity p. Reprinted with permission from [19], Copyright 2008, Wiley-VCH

q for $p = 0.1$, 0.3 and 0.5. The center position of the peak q_0 gives the dominant spatial correlation length $s = 2\pi/q_0$. The peak becomes broader at larger p. The full width at half maximum (FWHM) of the peak Δq gives the average size of ordered domains $\xi_q = 2\pi/\Delta q$. As shown in Fig. 9.2 (b), ξ_q decreases with increasing p, similar to ξ_r.

The radial distribution function $g(r)$, plotted in Fig. 9.3 (a) for several values of p, gives the probability for a cylinder to be located a distance r from another cylinder at the origin relative to that for an ideal gas. The strong first peak, splitting of the second peak, and existence of peaks at large r for $p = 0.1$ indicate that the structure possesses crystalline order. With increasing p, the peaks are broadened, decay faster with r, and $g(r)$ resembles that for a dense liquid [34].

In addition to the translational order, we also characterized the orientational order of the configurations. The bond-orientational order parameter ψ_6 measures the hexagonal registry of nearest neighbors [35]. ψ_6 can be calculated 'locally', which does not include phase information, or 'globally', which allows phase cancellations. Equations (9.4) and (9.5) provide expressions for the global and local bond-orientational order parameters in 2D structures.

$$\psi_6^g = \frac{1}{N}\left|\sum_{i=1}^{N}\frac{1}{m_i}\sum_{j=1}^{m_i} e^{6\imath\theta_{ij}}\right| \tag{9.4}$$

$$\psi_6^l = \frac{1}{N}\sum_{i=1}^{N}\frac{1}{m_i}\left|\sum_{j=1}^{m_i} e^{6\imath\theta_{ij}}\right|, \tag{9.5}$$

where θ_{ij} is the polar angle of the bond connecting the cylinder i to its neighbor j, and m_i denotes the number of nearest neighbors of i. Two cylinders are deemed

nearest neighbors if their center-to-center distance $r_{ij} < r_{\min}$, where $r_{\min}$ is the location of the minimum between the first two peaks in $g(r)$.

As shown in Fig. 9.3 (b), both ψ_6^l and ψ_6^g decrease as p increases. ψ_6^l is larger than ψ_6^g, because of the different orientations of the ordered domains. The error bars represent the standard deviations from 100 configurations. For $p = 0.1$, there is a significant fluctuation of ψ_6^g, because some configurations have only a few distinct domains while others contain many domains with different orientations. With increasing p, the number of domains N_d increases, thus the mean and standard deviation of ψ_6^g decrease. For $p = 0.5$, $\psi_6^g \approx 0$, the structures possess only local bond orientational order with $\psi_6^l \approx 0.55$ as found in dense liquids [35].

Density of Optical States

We calculate the DOS with transverse electric (TE) polarization using the order-N method [36]. The magnetic field is parallel to the axis of the air cylinders, and the electric field exists in the 2D plane. Since the cylinders are generated in a square with periodic boundary conditions, we can use it as a supercell for the DOS calculation. For the initial conditions, we choose a superposition of Bloch waves with random phases for the magnetic field and set the electric field to zero [37]. The temporal evolution of electromagnetic fields is obtained by solving the Maxwell's equations with the finite-difference time-domain (FDTD) method. We record the time series of fields at 400 positions which are randomly distributed across the structure, and Fourier transform them to the frequency domain. The sum of their Fourier intensities (i.e., spectral intensities) consists of a number of peaks that correspond to the resonant modes. Adding the contributions of many Bloch wave vectors and averaging over many configurations result in a smooth function for the DOS. We have tested our code by reproducing the DOS for two-dimensional photonic structures in the literature [37].

In Fig. 9.4, we plot the DOS as a function of the normalized frequency $\omega a/2\pi c = a/\lambda$ for the structures generated by the first protocol with $p = 0.1, 0.2, 0.3, 0.4$, and 0.5, and a triangular lattice ($p = 0$) with identical density and diameter air cylinders. The refractive index of the dielectric host in which the air cylinders are embedded is also varied with $n = 3.4$, 1.8, and 1.4 from left to right in Fig. 9.4. The values of n are taken from those of commonly used semiconductors, oxides and polymers. For $n = 3.4$ and $p = 0$, a complete depletion of the DOS from $a/\lambda = 0.235$ to 0.365 results from the full PBG between the first and second bands of the triangular lattice. With the introduction of positional disorder, defect modes are created inside the gap, and the frequency region of depleted DOS becomes shallower and narrower. The higher frequency side of the gap (air band edge) is affected more than the lower frequency side (dielectric band edge). Because the air holes are isolated and the dielectric host is connected, the dielectric bands below the gap are more robust to the disorder than the air bands above the gap. For $n = 1.8$, the PBG of the periodic structure becomes smaller, and thus the depleted region of the DOS is narrower. For the perfect crystal with $n = 1.4$, the first photonic band at the K point ($K1$) has the

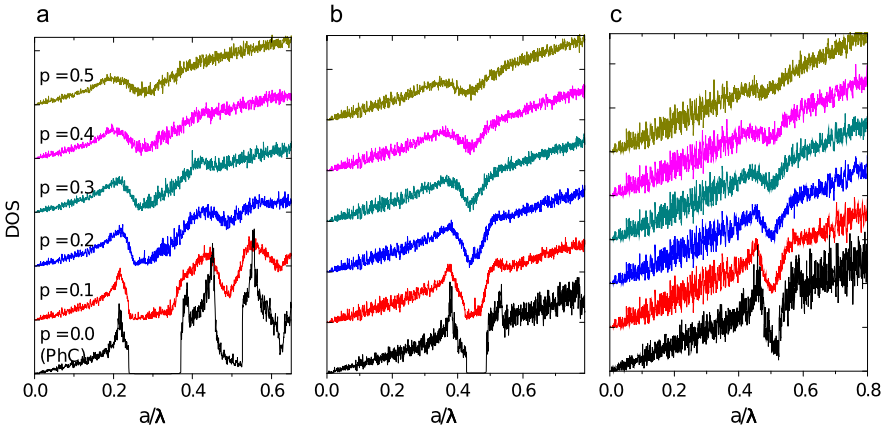

Fig. 9.4 Density of optical states (DOS) as a function of the normalized frequency $\omega a/2\pi c = a/\lambda$ for the 2D structures generated by the first protocol with $p = 0.1$, 0.2, 0.3, 0.4, and 0.5, and a triangular lattice ($p = 0$) of identical density and diameter of air cylinders. The dielectric media, in which the air cylinders are embedded, have refractive indexes (**a**) 3.4, (**b**) 1.8, and (**c**) 1.4. Reprinted with permission from [19], Copyright 2008, Wiley-VCH

same energy as the second band at the M point ($M2$), thus the full PBG disappears. As a result, the DOS displays a dip, rather than a complete depletion. As shown in Fig. 9.4, the addition of positional disorder causes the dip in the DOS to become shallower and eventually disappear at large disorder.

To quantify the strength of the DOS depletion, we introduce the normalized depth S, which is defined as the ratio of the maximal depth of DOS reduction to the DOS of a random structure at the same frequency. The density and diameter of air cylinders as well as the refractive index of the dielectric host in the random structure are identical to those of the structures under investigation. The DOS of the random structure increases almost linearly with frequency, similar to that of a homogeneous 2D dielectric medium. We investigated the dependence of S on various order parameters, e.g. the local bond orientational order ψ_6^l. S increases gradually with ψ_6^l. However, the variation depends on the refractive index contrast n, and is therefore not universal.

To obtain universal behavior for a given degree of positional order, we must account for the effect of refractive index contrast on the DOS. The refractive index contrast determines the strength of the PBG, which is reflected in the attenuation length of Bragg diffraction, or the Bragg length l_b. Roughly speaking, the Bragg length gives an order of magnitude estimate for the minimal size of a periodic structure that is necessary to form a PBG via Bragg scattering. Since periodic structures are anisotropic, l_b varies with direction. However, since the DOS is a sum of optical modes in all directions, the relevant Bragg length is an average over all directions. To obtain the value of l_b in the numerical simulations, we place a continuous dipole source of frequency ω_d in the middle of a large triangular array of air cylinders. We then calculate the electric field intensity at a distance r from the source, and inte-

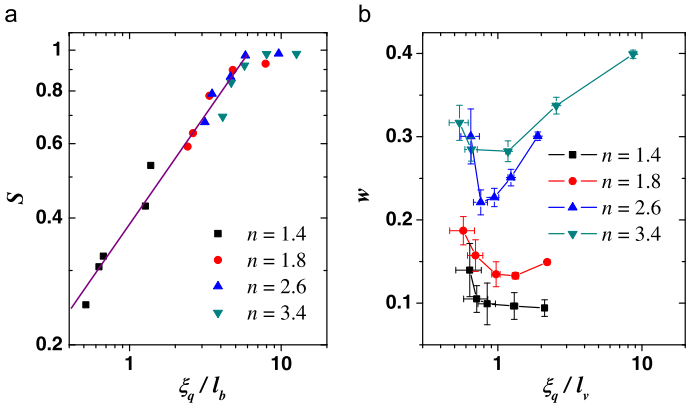

Fig. 9.5 (**a**) Normalized depletion depth of the DOS S for arrays of air cylinders in a dielectric host of refractive index n versus the ratio of the average domain size ξ_q to the angle-averaged Bragg length l_b. A linear fit (*solid gray line*) of the data on the log-log plot for $\xi_q / l_b \lesssim 5$ gives a power-law scaling exponent of 0.52. (**b**) Relative width w of the frequency region where there is a reduction in the DOS as a function of ξ_q / l_v, where l_v is the frequency- and angle-averaged Bragg length. The *error bars* are obtained from the standard deviation of ξ_q for different configurations and fitting errors in the FWHM of the DOS reduction zones. Reprinted with permission from [19], Copyright 2008, Wiley-VCH

grate it over the polar angle. The Bragg length l_b is extracted from the exponential decay of the angle-integrated field intensity I with r.

In Fig. 9.5 (a), we plot the depth S versus the average size of the ordered domains normalized by the Bragg length, ξ_q / l_b. All data points for different refractive index contrasts fall on a single curve. When ξ_q / l_b is above a threshold value ($\sim$5), S is almost unity, which implies that the depletion in the DOS is nearly complete as in a perfect crystal. When $\xi_q / l_b \lesssim 5$, S decreases rapidly. The drop can be fit by a straight line on a log-log plot, which reveals a power-law decay with an exponent $\sim$0.52. This result can be understood qualitatively as follows. If the domain size is larger than the Bragg length, Bragg scattering in a single domain is strong enough to form a PBG. The DOS in systems with large ξ_q / l_b is nearly equal to the DOS of a perfect crystal, and these structures can be regarded as photonic polycrystals. In addition, an average over many domains of different orientations makes the directional DOS isotropic. If the domain size is smaller than the Bragg length, individual domains are too small to form PBGs. In this case, the effect of Bragg scattering is reduced due to a limited number of periodic units, and the depletion of the DOS is weakened. This is the amorphous photonic regime, where short-ranged order leads to a partial depletion of the DOS. The well-defined threshold in ξ_q / l_b demonstrates a clear transition from polycrystalline to amorphous photonic structures.

In addition to the depth of the DOS reduction, we also studied the spectral width of the reduction region. The relative width w is defined as the ratio of the full width at half minimum (FWHM) of the dip in the DOS $\delta\omega$ to the frequency ω_0 at the center of the dip. Since the Bragg length varies within the spectral region of DOS reduction, we average its value over the frequency range from $\omega_0 - \delta\omega$ to $\omega_0 + \delta\omega$. The

average domain size is normalized by the average Bragg length l_v. Figure 9.5 (b) shows a plot of w versus ξ_q/l_v for several values of n. Although the curves for different n do not coincide, their trends are similar. As ξ_q/l_v increases, w first drops and then rises (except for $n = 1.4$). The turning point is at $\xi_q/l_v \sim 1$. To understand this behavior, we first examine the DOS for periodic systems. At $n = 3.4$, the DOS is enhanced at the photonic band edges due to the slow group velocity [Fig. 9.4 (a)]. When positional disorder is introduced to the structure, the DOS peak at the air band edge is quickly lowered and the higher frequency part of the PBG is filled by defect modes. In contrast, the peak at the dielectric band edge decreases more slowly, because the dielectric bands are more robust against disorder as mentioned earlier. The gap width is reduced, until the DOS peak at the dielectric band edge diminishes at a certain degree of disorder. Then the DOS below the dielectric band edge starts decreasing with further increases in disorder. The DOS reduction region becomes wider. As n decreases, the strength of DOS reduction by PBGs is weakened, and $\delta\omega/\omega_0$ is lowered. At $n = 1.4$, w no longer rises beyond $\xi_q/l_v \sim 1$; instead it tends to a plateau.

Enhanced Scattering and Mode Confinement by Short-Range Order

In nature, the refractive index contrast is typically low, nevertheless photonic amorphous structures are used to manipulate light scattering and color generation. In this section, we investigate the effects of short-range order on light scattering and mode confinement in amorphous structures with low index contrast. We consider the structures generated by the first protocol with $p = 0.5$. When we set $n = 1.4$, the DOS possesses an extremely shallow dip as shown in Fig. 9.6 (a). For $n = 1.2$, the DOS in Fig. 9.6 (e) is nearly featureless. We calculate the resonant modes in these structures using the finite element method. Instead of periodic boundary conditions, the structures have finite size and open boundaries. Each structure contains 1024 air cylinders in a dielectric medium. The open boundaries are terminated by perfectly matched layers that absorb all outgoing waves. Because of light leakage from the finite-sized structure, the resonant modes have finite lifetimes. We calculate the complex frequencies of all resonances $\omega_r + i\omega_i$. The amplitude of ω_i is inversely proportional to the lifetime. The quality factor is defined as $Q = \omega_r/2|\omega_i|$. We obtain the maximal quality factors Q_m of modes within small frequency intervals, and plot them in Fig. 9.6 (b, f). Although the dip in the DOS is barely visible at $n = 1.4$, Q_m is enhanced by a factor of three at a frequency near the center of the dip. Further, even though there is essentially no dip in the DOS for $n = 1.2$, Q_m displays a peak. Figure 9.6 (d, h) shows the spatial distributions of electric field intensities $|E(x, y)|^2$ for the modes with maximal Q_m (marked by the arrows in Fig. 9.6 (b, f)). It is evident that the mode of maximal Q_m at $n = 1.4$ is localized within the structure. For $n = 1.2$ the mode is more delocalized, but the field intensity near the boundary (marked by white dashed line) is still weaker than that in the interior. To determine the degree of localization, we calculate the mode size which is inverse of the inverse

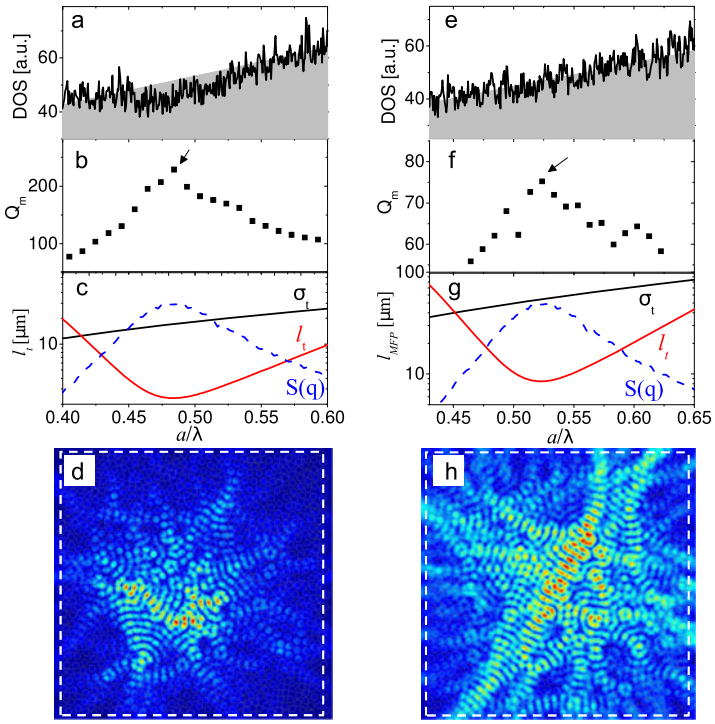

Fig. 9.6 The DOS (**a**, **e**) and maximal quality factors Q_m of resonant modes (**b**, **f**) for the amorphous photonic structures with low refractive index contrast $n = 1.4$ for (**a**–**d**) and 1.2 for (**e**–**h**). *Grey backgrounds* in (**a**, **e**) represent the DOS for 2D homogeneous media. (**d**, **h**) Spatial distribution of electric field intensities for the modes of maximal Q_m [marked by *arrows* in (**b**, **f**)]. (**c**, **g**) Transport mean free path l_t (*solid line*), total scattering cross sections of a single scatterer σ_t (*dashed line*), and the structure factor $S(q)$ at $q = 2k$ (*dotted line*), where k is the wavevector of light. Reprinted with permission from [19], Copyright 2008, Wiley-VCH

participation ratio,

$$s \equiv \frac{1}{L^2} \frac{(\int |E(x,y)|^2 \, dx\, dy)^2}{\int |E(x,y)|^4 \, dx\, dy}, \tag{9.6}$$

where a mode uniformly distributed over the sample gives $s = 1$. We find that the mode in Fig. 9.6 (d) has $s = 0.18$ and is thus highly localized, while the one in Fig. 9.6 (f) has $s = 0.44$ and is only partially localized.

To illustrate the physical mechanism that leads to mode confinement, we calculate the transport mean free path

$$\frac{1}{l_t} = \frac{\pi}{k^6} \int_0^{2k} \rho F(q) S(q) q^3 \, dq, \tag{9.7}$$

where k is the wavevector of light, ρ is the number density of air cylinders, $S(q)$ is the structure factor, $F(q)$ is the form factor, and q is the spatial frequency. $F(q)$

is given by the differential scattering cross section of a single air cylinder in the dielectric medium. The structure factor is given by

$$S(\mathbf{q}) \equiv \frac{1}{N} \sum_{i,j=1}^{N} e^{i\mathbf{q}\cdot(\mathbf{r}_i - \mathbf{r}_j)}, \tag{9.8}$$

where $\mathbf{r}_i$ denotes the center position of the ith cylinder. Since the structures are isotropic, $S(\mathbf{q})$ is invariant with the direction of $\mathbf{q}$ and is only a function of the magnitude q. In Fig. 9.6 (c, g), we show that l_t displays a significant drop at a frequency that coincides with the peak in Q_m. This indicates that the enhancement of scattering strength improves mode confinement. In Fig. 9.6 (c, g) we also plot the total scattering cross section σ_t of a single air cylinder, which increases monotonically with frequency and does not exhibit any resonant behavior within the frequency range studied. This behavior suggests that the dip in l_t is not caused by Mie resonance of individual scatterers. Instead, we contend that the short-range order enhances Bragg backscattering at certain wavelengths and shortens l_t. To prove this, we also plot $S(q)$ for the backscattering $q = 2k$ in Fig. 9.6 (c) and (g). $S(q)$ is peaked near the dip of l_t, which confirms that collective backscattering from local domains of ordered cylinders causes a dramatic decrease in l_t. Therefore, the spatial confinement of resonant modes is enhanced by short-range order through constructive interference of scattered light that occurs at specific frequencies.

9.2.2 *Lasing in Photonic Polycrystalline and Amorphous Structures*

Next we present the experimental study on lasing characteristics in photonic polycrystalline and amorphous structures.

Sample Fabrication and Lasing Experiment

The computer generated patterns of polycrystalline and amorphous arrays of circular holes were transferred to a GaAs membrane. A 190-nm-thick GaAs layer and a 1000-nm thick $Al_{0.75}Ga_{0.25}As$ layer were grown on a GaAs substrate by molecular beam epitaxy. Inside the GaAs layer there were three uncoupled layers of InAs QDs equally spaced by 25 nm GaAs barriers. 2D arrays of cylinders were written on a 300-nm-thick ZEP layer with the electron-beam lithography. The patterns were transferred to the GaAs layer by chlorine-based inductive-coupled-plasma reactive-ion-etching with the ZEP layer as a mask. The ZEP layer was subsequently removed in an oxygen plasma cleaning process. Finally the $Al_{0.75}Ga_{0.25}As$ layer was selectively removed by a dilute HF solution. Figure 9.7 (a, b) shows the top-view scanning electron microscope (SEM) images of two fabricated patterns. The lateral dimension of a pattern is 9.3 μm, and it has 1024 air holes. The radius of air holes r

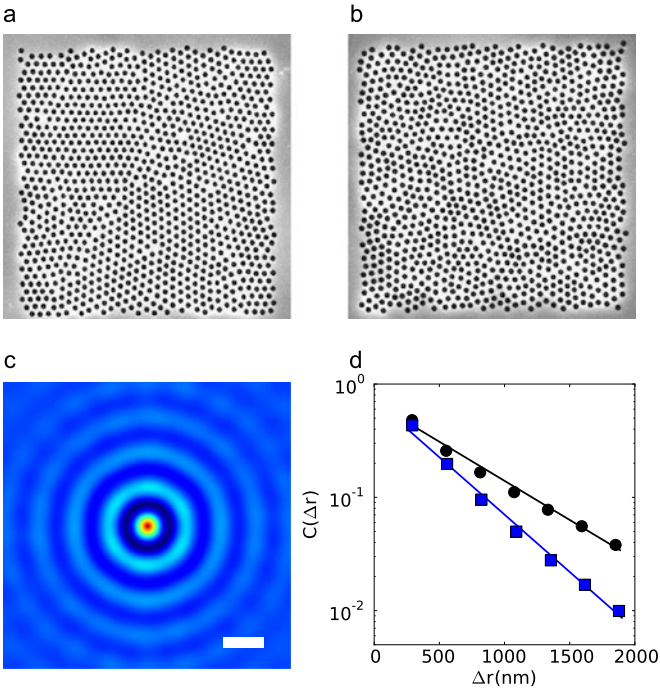

Fig. 9.7 (**a**, **b**) Top-view SEM images of fabricated arrays of air holes in a GaAs membrane. The *scale bar* is 2 μm. Ordered domains of different orientations can be seen in (**a**), but barely in (**b**). (**c**) 2D spatial correlation function $C(\Delta\mathbf{r})$ averaged over five configurations including the pattern in (**b**) and equivalent ones. *Scale bar* = 300 nm. (**d**) Log-linear plot of the peak amplitude of azimuthal-averaged spatial correlation function $C(\Delta r)$, *squares* for the pattern in (**a**), and *circles* for (**b**). The *straight lines* are exponential fit, giving the decay length $\xi = 2.3$a for (**a**) and 1.4a for (**b**). Reprinted with permission from [21], Copyright 2008, Wiley-VCH

is 100 nm. In the pattern of Fig. 9.7 (a), we can clearly see domains of the triangular lattice of holes, each domain has a different orientation. In Fig. 9.7 (b), the domains are so small that barely visible.

For qualitative understanding of the short-range order, the 2D spatial correlation function $C(\Delta\mathbf{r})$ for these patterns were calculated. A typical ensemble-averaged $C(\Delta\mathbf{r})$ is presented in Fig. 9.7 (c). It consists of rings whose amplitudes decrease with increasing spatial separation $\Delta r \equiv |\Delta\mathbf{r}|$. Since $C(\Delta\mathbf{r})$ is isotropic, we calculated the azimuthal-averaged $C(\Delta r)$ for the two patterns in (a, b) and plotted the peak amplitudes in Fig. 9.7 (d). The first peak away from $\Delta r = 0$ is produced by the nearest cylinder, thus its position corresponds to the average spacing a of the nearest neighbors. The two patterns in Fig. 9.7 (a, b) have $a = 290$ nm. The faster damping of $C(\Delta r)$ for the pattern in Fig. 9.7 (b) reflects the spatial correlation is shorter-ranged. They both fall on straight lines in a log-linear plot, indicating exponential decays. The decay length $\xi = 2.3a$, and $1.4a$ for the patterns in Fig. 9.7 (a, b). Ac-

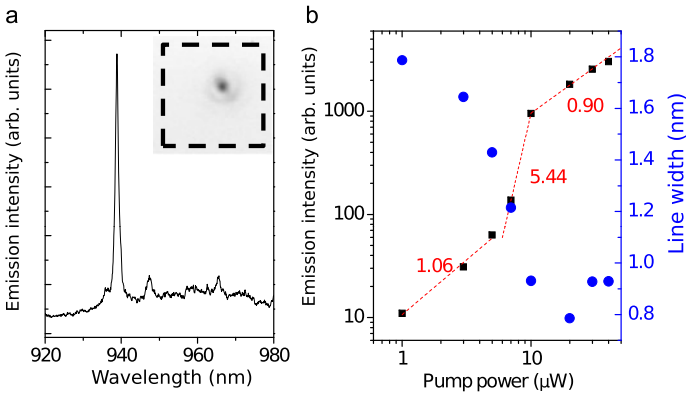

Fig. 9.8 (**a**) Measured spectrum of emission from a pattern of $\xi = 4.4a$ and $a = 290$ nm at the incident pump power $P = 30$ μW. The *inset* is an optical image of the lasing mode corresponding to the sharp peak in the emission spectrum. *Black dashed square* marks the pattern boundary. (**b**) Intensity I (*black square*) and width $\Delta\lambda$ (*blue circle*) of the lasing peak in (**a**) versus the incident pump power P in a logarithmic plot. The *red dotted lines* represent linear fit of $\log I$ vs. $\log P$ in three regimes, and the numbers next to them are those slopes. Reprinted with permission from [21], Copyright 2008, Wiley-VCH

cording to our previous study [19] and the calculation results in the next section, the pattern in Fig. 9.7 (a) is polycrystalline and (b) amorphous.

In the lasing experiments, the samples were cooled to 10 K in a continuous-flow liquid Helium cryostat, and optically pumped by a mode-locked Ti:Sapphire laser (pulse width ~200 fs, center wavelength ~790 nm, and pulse repetition rate ~76 MHz). A long working distance objective lens (numerical aperture =0.4) focused the pump light to a pattern at normal incidence. The diameter of pump spot on the sample surface was about 2 μm. The emission from the sample was collected by the same objective lens. The emission spectrum was measured by a high resolution spectrometer with a liquid-nitrogen-cooled coupled-charged-device (CCD) array detector. Simultaneously the spatial distribution of emission intensity across the sample surface was projected onto a thermoelectric-cooled CCD camera.

Figure 9.8 (a) is part of a time-integrated spectrum of emission from a polycrystalline pattern ($\xi/a = 4.4$, $a = 290$ nm). It features a sharp peak on top of a broad QD emission band. Figure 9.8 (b) plots the intensity I and linewidth $\Delta\lambda$ of this peak as a function of the incident pump power P. The variation of $\log I$ with $\log P$ exhibits a S-shape with two kinks. The slopes in the three regimes separated by the two kinks were obtained from curve fitting and written on the graph. In the first and last regimes, the slopes of $\log I$ over $\log P$ are very close to unity, indicating a linear growth of I with P. The second regime has a slope of 5.44, meaning I scales as $P^{5.44}$. The first regime corresponds to spontaneous emission of QDs to a resonant mode, thus the intensity increases linearly with the pump power. When the pump is high enough, the emission peak grows superlinearly as a result of light amplification by stimulated emission. This is the second regime. In the third regime, lasing occurs in this mode, and the gain saturation reduces the slope to one. Also

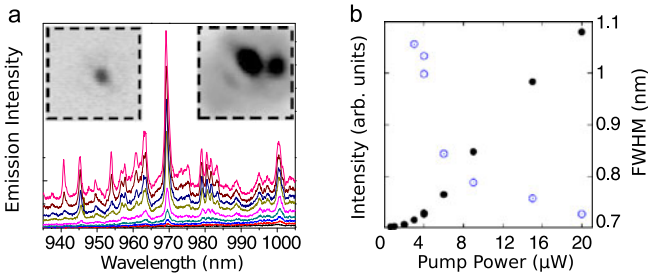

Fig. 9.9 (**a**) Evolution of emission spectra of a pattern with $\xi/a = 1.4$ and $a = 270$ nm as the pump power increases (*from bottom to top*). *Inset* is an optical image of the lasing mode at $\lambda = 970$ nm. (**b**) Intensity and width of the emission peak at $\lambda = 970$ nm as a function of the pump power. Reprinted with permission from [21], Copyright 2008, Wiley-VCH

seen in Fig. 9.8 (b), the spectral width $\Delta\lambda$ of the peak first drops quickly with increasing P, then levels off and increases slightly at higher P. The rapid decrease of $\Delta\lambda$ is expected at the onset of lasing oscillation. The gradual increase above the lasing threshold results from the hot carrier effect. Due to the short pulse pumping, the carrier density keeps changing in time. It causes a temporal change of the refractive index, and consequently a continuous red-shift of lasing frequency [38, 39]. In our time-integrated measurement of lasing spectrum, the transient frequency shift results in a broadening of the lasing line. Such broadening increases with the hot carrier density and becomes dominant at high pumping level. The inset of Fig. 9.8 (a) is an optical image of the lasing mode, revealing its strong localization inside the pattern whose boundary is marked by the black dashed line.

We also realized lasing in photonic amorphous structures. As seen in Fig. 9.9 (a), there are many peaks of comparable height in the emission spectra of a pattern with $\xi = 1.4a$. Figure 9.9 (b) is a plot of the intensity and width of an emission peak at $\lambda = 970$ nm versus the pump power. The rapid increase of peak intensity and dramatic reduction of the peak width illustrates the onset of lasing action. A tunable interference filter was placed in front of the CCD camera to select this lasing mode for imaging. Inset of Fig. 9.9 (a) are the optical images of two lasing modes. The left one is spatially localized inside the pattern whose boundary was drawn by the dashed line. The double-peaked intensity distribution of the mode on the right is similar to that of a 2D necklace state in [40], suggesting it is a hybrid of two localized states. Further study is needed to confirm it is a necklace state [40, 41].

As we moved the pump beam spot across a pattern, new lasing peaks replaced the existing ones, and they have distinct frequencies. This phenomena indicate that resonant modes are localized in different positions of the samples, and brought to lasing when overlapped with the pump spot. We repeated the lasing experiment on several patterns with different arrangement of air holes but same ξ/a, and found the lasing peaks varied from pattern to pattern. We measured the patterns of different ξ/a and recorded the lasing wavelengths. Figure 9.10 plots the wavelengths of lasing peaks for five values of ξ/a. For a fixed ξ/a, there is a wide spread of lasing

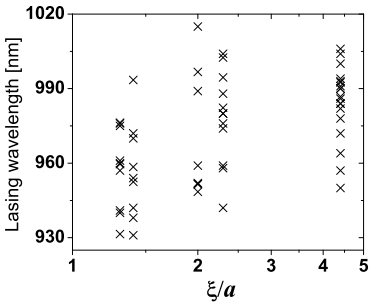

Fig. 9.10 Measured wavelengths of lasing peaks for patterns of different domain size ξ. The average spacing of nearest-neighboring air holes is $a = 290$ nm. Reprinted with permission from [21], Copyright 2008, Wiley-VCH

wavelengths due to the broad QD gain spectra. Nevertheless, it is evident that the lasing peaks shift to shorter wavelength as the average domain size ξ decreases.

Numerical Simulation of Lasing Modes

To explore the nature of lasing modes in photonic polycrystalline and amorphous structures, we performed numerical simulation. The perforated GaAs membrane is approximated as a 2D array of infinitely long air cylinders embedded in a uniform dielectric host with an effective index of refraction n_w. The value of n_w was obtained in the following steps. First we calculated the photonic band structure of a triangle lattice of air holes in a free-standing GaAs membrane of thickness 190 nm using the plane wave expansion method [42]. The density and size of air holes were identical to those of the fabricated samples. Next we calculated the photonic band structure of the approximate 2D system with n_w as a parameter. By adjusting the value of n_w, we matched the center frequency of the fundamental PBG obtained in the above two cases. In our calculation, we considered only the transverse-electric (TE) polarization (electric field perpendicular to the air cylinder axis), because experimentally the laser emission is TE polarized due to stronger gain of the InAs QDs for the TE polarized light.

Using the finite-difference frequency-domain (FDFD) method, we calculated the resonant modes with long lifetime in the passive structures. Due to the finite size of a pattern, light may escape through the open boundary. The outgoing wave is absorbed by the perfectly matched layer that surrounds the pattern. The resonant modes have finite lifetime, and their frequencies are complex numbers $\omega_r + i\omega_i$. The magnitude of ω_i is inversely proportional to the mode lifetime. The quality factor is defined as $Q = \omega_r/2|\omega_i|$. We calculated the complex frequencies of TE modes, and found the highest quality factor Q_m within small frequency bins. Figure 9.11 (a) plots Q_m versus the normalized frequency a/λ for $\xi/a = 2.3$ and 1.4. Q_m drops quickly as ξ/a decreases. Nevertheless, it reaches the maximum at the same frequency $a/\lambda = 0.3$ for different ξ/a. This result can be explained by the DOS shown in Fig. 9.11 (b). For $\xi/a = 2.3$, there is a significant depletion of DOS, almost comparable to that of a PhC. The system can be regarded as a photonic polycrystal, as individual domains are large enough to form the PBG via Bragg scattering. Defect modes are formed

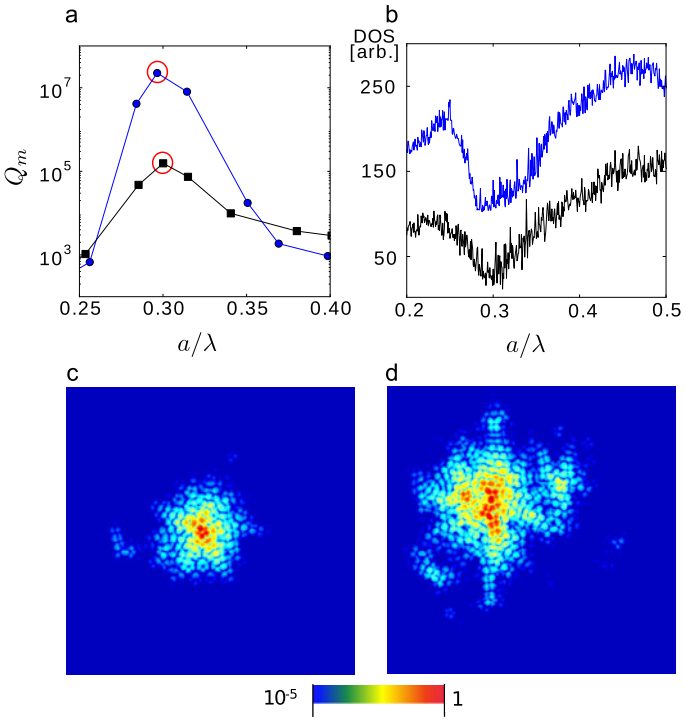

Fig. 9.11 (**a**) FDFD calculation of approximate 2D structures ($n_w = 2.73$) giving the maximal quality factor Q_m versus the normalized frequency a/λ for $\xi/a = 2.3$ (*blue circle*) and 1.4 (*black square*). (**b**) Calculated DOS for $\xi/a = 2.3$ (*top*) and 1.4 (*bottom*). The curves are shift vertically for clarification. Calculated spatial intensity distribution of the highest-Q_m mode for $\xi/a = 2.3$ (**c**) and 1.4 (**d**). They are marked with *circles* in (**a**). Reprinted with permission from [21], Copyright 2008, Wiley-VCH

inside the PBG. The closer their frequencies to the center of PBG, the higher their quality factors. Therefore, the highest-Q resonances in the photonic polycrystal are defect modes. They are strongly localized in space, as can be seen from a typical mode profile in Fig. 9.11 (c). The mode size, computed from the inverse participation ratio of the field distribution, is about 0.6 μm. When ξ/a is reduced to 1.4, Bragg scattering from each domain is not enough to produce a PBG. Consequently, the DOS has a dip instead of a gap. In this photonic amorphous structure, the peak of Q_m coincides with the dip of DOS. The reduction in DOS results from the short-range order, which enhances optical confinement and produces the maximum of Q_m [19, 20]. It leads to the maximum of Q_m. The spatial profile of a typical high-Q resonance is shown in Fig. 9.11 (d). The mode size is about 1.0 μm, much smaller than the lateral size of the structure (9.3 μm). This means the mode is still localized spatially, but the degree of localization is less than the defect mode in a polycrystal [Fig. 9.11 (c)]. The maximal Q_m drops quickly as the average domain size ξ decreases.

In our experiment the optical gain is distributed nonuniformly across the sample, because the pump spot diameter (∼2 μm) is smaller than the lateral dimension of the pattern (9.2 μm). Only the QDs inside the pump area are excited and provide optical gain. When light scattering is weak, the lasing modes may be very different from the resonant modes of the passive systems [43–45]. However, our samples have strong scattering, the transport mean free path is estimated [46] at $a/\lambda = 0.30$ to be 0.36 μm in the polycrstalline sample ($\xi/a = 2.3$) and 0.53 μm in the amorphous structure ($\xi/a = 1.4$). We extracted the localization length ξ_L in these structures by placing a monochromatic source at the center and calculating the steady-state field distribution. From the decay of the field intensity away from the source, we get $\xi_L = 0.38$ μm at $a/\lambda = 0.30$ in the sample of $\xi/a = 2.3$, and 0.46 μm in the sample of $\xi/a = 1.4$. Since the localization length is much smaller than the system size, the resonant modes are strongly confined within the structures. The typical size of high-Q modes is smaller than or comparable to the pump spot size, thus the lasing modes correspond to the high-Q modes inside the pump area.

According to the 2D calculation results, the frequencies of the highest-Q modes are the same for polycrystalline and amorphous structures, thus the lasing modes should not shift in frequency as ξ changes. This prediction contradicts the experimental data in Fig. 9.10, because light leakage in the third dimension is ignored in the calculation of 2D structures. Although light is confined in the free-standing GaAs membrane by index guiding, it can escape from the top or bottom surfaces of the membrane to the surrounding air. To account for this leakage, we performed the three-dimensional (3D) finite-difference time-domain (FDTD) calculation. The structural parameters used in the calculation are identical to those of the fabricated samples.

We calculated the high-Q resonances of TE polarization in the absence of gain or absorption. The quality factors Q_t of all modes within the frequency range of interest were found and plotted versus the normalized frequency a/λ in Fig. 9.12 for $\xi/a = 2.3$ and 1.4. The values of Q_t are orders of magnitude lower than those in Fig. 9.11 (c) for the same value of ξ/a. This result illustrates that the vertical leakage of light is much larger than the lateral leakage for the high-Q resonances. Such strong vertical leakage results from tight confinement in the lateral dimension. Namely, spatial localization of a mode in the xy-plane (parallel to the membrane) results in a broad distribution of in-plane wavevector $\mathbf{k}_{||}$ (projection of $\mathbf{k}$ vector to the xy-plane). The $\mathbf{k}_{||}$ components within the light cone ($|\mathbf{k}_{||}| \leq \omega/c$) can escape from the membrane in the $\pm z$ directions (normal to the membrane). The vertical leakage rate is characterized by the out-of-plane energy loss per optical cycle Q_v^{-1}, and the lateral by Q_h^{-1}. The total loss is described by $Q_t^{-1} = Q_h^{-1} + Q_v^{-1}$.

For the amorphous structure of $\xi/a = 1.4$, the mode of maximal Q_t at $a/\lambda \simeq 0.32$ has $Q_h = 4.88 \times 10^4$, and $Q_v = 1.62 \times 10^3$. Thus, the vertical leakage rate is an order of magnitude larger than the lateral one. In a polycrystalline structure, the tighter in-plane confinement of defect modes within the PBG makes the vertical leakage even stronger. Consequently, the modes at the center of PBG no longer have the highest Q_t, even though their Q_h is maximal. The highest Q_t modes are away from the PBG center, as shown in Fig. 9.12 for $\xi/a = 2.3$. These modes are less

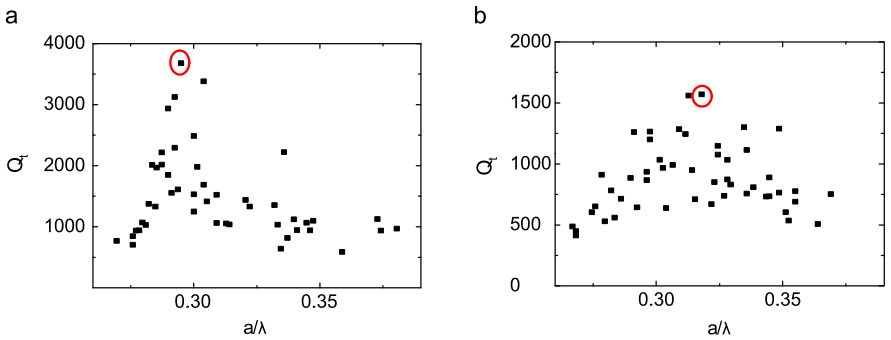

Fig. 9.12 3D FDTD calculation of resonances in the perforated GaAs membrane giving their quality factor Q_t as a function of the normalized frequency a/λ for $\xi/a = 2.3$ (**a**) and 1.4 (**b**). Reprinted with permission from [21], Copyright 2008, Wiley-VCH

confined in-plane, meaning their Q_h is lower. The larger spread in the xy-plane narrows the $\mathbf{k}_{||}$ distribution. The $\mathbf{k}_{||}$ components within the light cone is reduced, so is the out-of-plane leakage. The maximal-Q_t mode at $a/\lambda = 0.3$ has $Q_h = 7.55 \times 10^4$, and $Q_v = 3.87 \times 10^3$. Although its Q_h is lower than that of the defect modes at $a/\lambda = 0.32$ (PBG center), the Q_v is higher, so is the Q_t. Intuitively, the mode at the higher frequency side of the PBG center, i.e., at $a/\lambda = 0.34$, should have comparable Q_t to the maximal-Q_t mode at the lower frequency side ($a/\lambda = 0.30$), as their spectral distance to the PBG center is the same. However, the Q_t is lower at $a/\lambda = 0.34$, as seen in Fig. 9.12. This is because the air holes are isolated and the dielectric medium is connected in the membrane. The dielectric band edge at the lower frequency side of PBG is more robust to disorder, as evident in the DOS shown in Fig. 9.11 (b). Consequently, light confinement is stronger in the lower frequency part of the PBG, giving higher Q_t at $a/\lambda = 0.3$.

The 3D numerical simulation reveals that the maximal-Q_t modes shift to higher frequency as ξ decreases. This prediction agrees with the experimental observation that the wavelengths of lasing modes decreases from polycrystalline to amorphous patterns.

Control of Lasing with Short-Range Order

To characterize the effect of short-range structural order on lasing, we can either measure the threshold of individual lasing modes at different wavelength, or compare the intensity of different lasing modes at the same pumping level. In principle, the spectral variation of gain coefficient and mode competition for gain would influence the lasing threshold and emission intensity. However, the gain spectrum of InAs QDs is very broad, and the gain coefficient has little variation over a wide spectral range. More importantly, the gain spectrum is dominated by inhomogeneous broadening, which significantly weakens mode competition. Hence, the interaction of lasing modes at different wavelength or spatial location is negligible. To increase

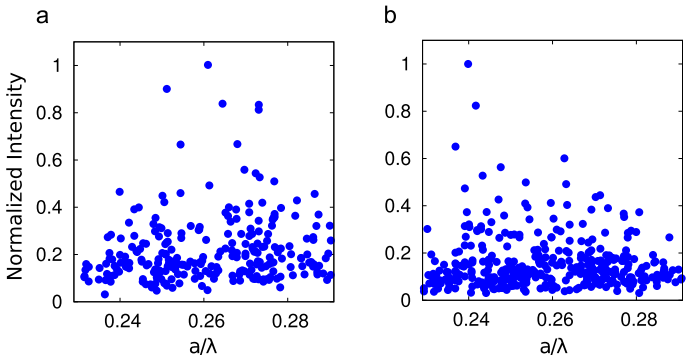

Fig. 9.13 Measured intensities of lasing peaks from three PAS of $a = 235$ nm, 255 nm and 275 nm. The air filling fraction $f = 0.33$ in (**a**) and 0.28 in (**b**). Laser emission intensity reaches the maximum at the normalized frequency $a/\lambda = 0.26$ in (**a**) and 0.24 in (**b**). Reprinted with permission from [20], Copyright 2008, Wiley-VCH

the range of normalized frequency $\omega a/2\pi c = a/\lambda$, we probe lasing in multiple arrays of distinct a. The ratio of r over a is kept constant, so that the filling fraction f of air does not change. Figure 9.13 (a) plots the intensities of numerous lasing modes collected from three arrays of $a = 235$ nm, 255 nm and 275 nm. The incident pump power is fixed at 16 μW. The pump spot is scanned across the interior of each array to probe lasing modes at different locations. The size of pump spot is kept at 1.2 μm. The range of a/λ, covered by the three patterns, is from 0.23 to 0.29. As a/λ increases, the lasing mode intensity first increases and then decreases. It reaches the maximum at $a/\lambda = 0.26$. Thus lasing becomes the strongest, or equivalently the lasing threshold is the lowest at $a/\lambda = 0.26$. Next we change the air filling fraction f from 0.33 to 0.28 by varying r/a, and measure three samples of $a = 235$ nm, 255 nm and 275 nm. As shown in Fig. 9.13 (b), the maximum intensity of lasing modes is shifted to $a/\lambda = 0.24$. These results confirm that there exists an optimal frequency for lasing in the PAS, and its value can be tuned by the structural parameters.

To interpret the experimental data, we calculate the quality (Q) factor of resonant modes in the samples. The higher the Q factor, the longer the photon lifetime in the PAS, the stronger the amplification of light. We use the finite-difference frequency-domain (FDFD) method in the numerical simulation. Since the 3D FDFD calculation is computationally expensive, we calculate the resonant modes in the approximate 2D structures. More specifically, we first compute the effective refractive index n_w of the waveguided mode in the GaAs layer free standing in air. We consider only the transverse-electric (TE) polarization (electric field parallel to the GaAs layer), because the laser emission is TE polarized. Then the value of n_w as a function of λ is assigned to the refractive index of the dielectric host in which the air cylinders are embedded. The air cylinders are assumed to be infinitely long in the 2D FDFD calculation. Figure 9.14 (a) plots Q vs. a/λ for three PAS of $f = 0.33$. The values of a and r are equal to those of the fabricated samples. The Q factor is peaked at

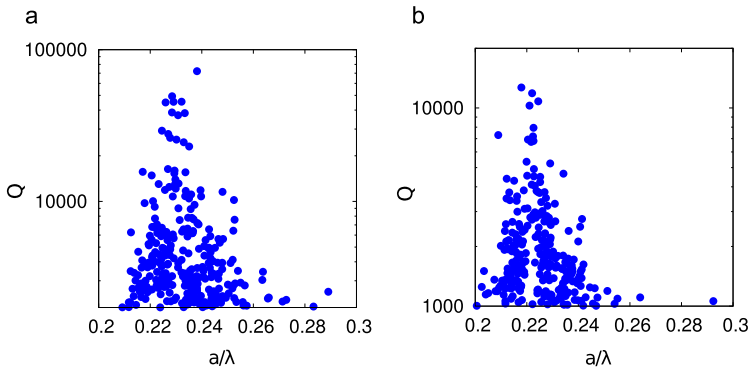

Fig. 9.14 Calculated Q factor of resonant modes in the PAS whose structural parameters are identical to those in Fig. 9.13 (a) and (b). As the air filling fraction f changes from 0.33 (**a**) to 0.28 (**b**), the maximum of Q factor shifts to lower normalized frequency a/λ. Reprinted with permission from [20], Copyright 2008, Wiley-VCH

$a/\lambda = 0.24$. When the air filling fraction f is changed to 0.28, the maximum of Q factor shifts to a lower frequency (Fig. 9.14 (b)). These trends agree qualitatively to those of laser emission intensity measured experimentally (Fig. 9.13). The maxima occur at slightly different frequencies, due to 2D approximation in the numerical simulation and uncertainty in determining the refractive index of GaAs at low temperature. Note that the 2D simulation only takes into account light leakage through the edges of an array. Experimentally, light can also escape through the top or bottom surface of the GaAs membrane to air. The vertical leakage is included in our finite-difference time-domain (FDTD) simulation of a free-standing GaAs membrane. For the PAS, the total Q factor (including both lateral and vertical leakage) displays a similar trend to that in Fig. 9.13. However, the actual Q value is notably lower than that in Fig. 9.14 as a result of the vertical leakage. Hence, the variation of Q with a/λ is determined by the lateral leakage. The existence of Q maximum indicates light confinement is the strongest at specific wavelength λ that scales with the characteristic length scale a of the structure. Thus the Q enhancement originates from the short-range order. Since stronger optical confinement increases the dwell time of light in the structure, light experiences more amplification and the lasing threshold is reduced. In other words, the maximum of the Q factor leads to a minimum of the lasing threshold, or equivalently, a maximum of laser emission intensity at a fixed pump power above the threshold.

To confirm the origin of Q enhancement, we estimate the transport mean free path l_t, which is a measure of the scattering strength. For the approximate 2D structure,

$$l_t(\lambda) = \left(\frac{\pi}{k^6} \int_0^{2k} \rho F(q) S(q) q^3 \, dq \right)^{-1}, \tag{9.9}$$

where q is the spatial frequency of the structure, $F(q)$ is the form factor, $S(q)$ is the structure factor, ρ is the density of scatterers, and k is the wave vector [47].

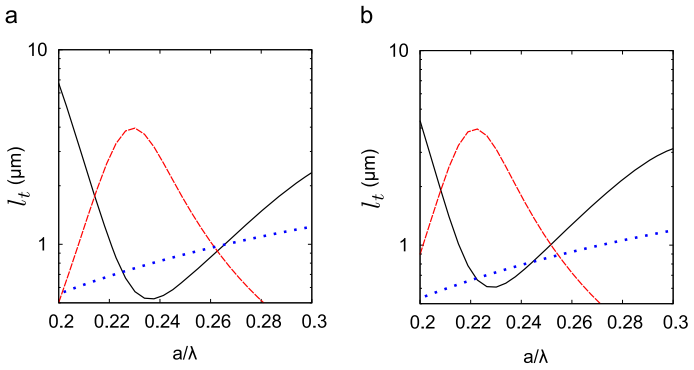

Fig. 9.15 (**a**) Estimated transport mean free path l_t (*black solid curve*) as a function of the normalized frequency a/λ in the PAS of air filling fraction $f = 0.33$ (**a**) and 0.28 (**b**). *Red dashed curve* is the structure factor $S(q = 2k)$ of PAS, and the *blue dotted curve* the total scattering cross section σ_t of a single air cylinder embedded in a dielectric host. σ_t does not exhibit any Mie resonance. The dip in l_t almost coincides with the peak in $S(q)$, confirming the enhanced light scattering is caused by short-range order

$k = 2\pi n_e/\lambda$, where λ is the wavelength in vacuum, and n_e is the effective index of refraction of the 2D structure. If the structure is completely random, $S(q)$ becomes 1. For the PAS, we compute the structure factor from the center positions of air holes. Since the structure is isotropic, S depends only on the magnitude of $\mathbf{q}$. $F(q)$ is obtained from the differential scattering cross section of a single air cylinder (infinitely long) embedded in a dielectric host of refractive index n_w. n_e is estimated by the Maxwell-Garnett formula with the air filling fraction f.

Figure 9.15 (a) plots l_t (black solid curve) as a function of a/λ for the PAS of $f = 0.33$. It has a significant dip at $a/\lambda = 0.24$, where light scattering becomes the strongest. The minimum of l_t almost coincides with the maximum of Q in Fig. 9.14 (a), indicating the optimal light confinement is caused by the strongest scattering. To find the origin of enhanced light scattering, we plot the total scattering cross section σ_t of a single air cylinder (blue dotted curve) in Fig. 9.15 (a). It increases monotonically with a/λ, and does not exhibit any resonant behavior within the frequency range of study. Hence, the dip in l_t is not caused by any Mie resonance of individual scatterers. In the same figure we also plot $S(q)$ for the backscattering $q = 2k$. Its value is peaked near the dip of l_t, confirming the short-range order enhances backscattering and shortens l_t [29]. Similar results are obtained for the PAS of $f = 0.28$ [Fig. 9.15 (b)]. The dip of l_t moves to lower frequency, consistent with the shift of Q maximum [Fig. 9.14 (b)] and the strongest laser emission intensity [Fig. 9.13 (b)]. Note that in the estimation of l_t with (9.1), the near-field coupling of adjacent scatterers is neglected. Within the frequency range of interest, there is no scattering resonance of individual air cylinders, thus the coupling of neighboring cylinders via evanescent wave is weak.

9.3 Photonic Network Structures and Lasers

The photonic amorphous structures have two types of topology: (i) an aggregate of dielectric spheres/cylinders, (ii) a continuous network of dielectric material. The photonic bandgaps can be formed in (i) via evanescent coupling of Mie resonances of individual scatterers [10–14, 18]. However, two-dimensional and three-dimensional (3D) realizations of (ii) can possess larger PBGs [16, 17, 48] For example, a photonic amorphous diamond structure formed by a 3D network of silicon has a 18 % PBG [16, 48]. Since the PAS is isotropic, the PBG is identical in all directions. The photonic bandedge (BE) modes can be strongly localized without introducing any defect in a PAS [17, 18, 48]. It is dramatically different from a periodic structure where the PBG is anisotropic and the BE modes are spatially extended.

Most studies on amorphous network structures have focused on passive systems that have no gain or nonlinearity. What happens if we introduce optical gain to the 2D amorphous network structures? Can we achieve lasing? What are the lasing modes? These questions will be addressed in the section.

9.3.1 2D Photonic Network Laser

To generate a 2D trivalent network structure (each junction having three bonds), we first created a jammed packing of polydisperse cylinders in a computer simulation [19]. The center positions of cylinders are marked by black solid circles in Fig. 9.16 (a). Then we performed a Delaunay tessellation that provides triangular partitioning (blue thin lines) [17]. Associated with each triangle is a centroidal point. We connected the centroids of neighboring triangles with line segments. The resulting structure is a trivalent network shown in red thick lines. The spatial Fourier spectra of the structure [inset of Fig. 9.16 (b)] exhibits a circular ring pattern, indicating the structure is isotropic and there exits a dominant spatial frequency that corresponds to the radius of the ring. We also calculated the 2D spatial correlation function $C(\Delta r)$, which is plotted in Fig. 9.16 (b). The characteristic length scale of the structure a is obtained from the first peak of the correlation function. The rapid decay of the amplitude of $C(\Delta r)$ with Δr reveals the structural correlation is short-ranged.

As to be detailed later, we fabricated 2D trivalent network structures in a GaAs membrane that was 190 nm thick and free-standing in air. To obtain the effective index of refraction n_e of the GaAs segments for the 2D simulation, we computed the fundamental PBG in a triangle lattice of air holes in a free-standing GaAs membrane (using the plane wave expansion method), then adjusted n_e of an approximate 2D structure to get a similar PBG. The value of n_e depends on the filling fraction of air in the GaAs membrane f, which is chosen to be 0.53 to have the maximal PBG. The 2D network structure was assigned the same $f = 0.53$ and $n_e = 2.68$. We calculated the 2D density of optical states (DOS) using the order N method in

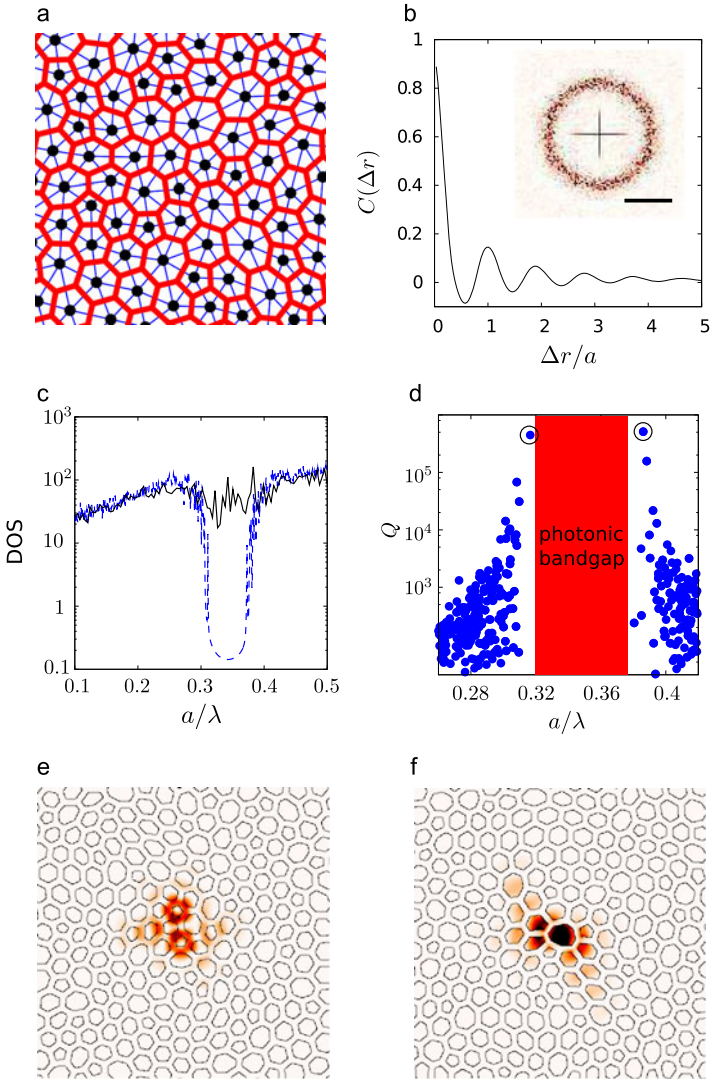

Fig. 9.16 (**a**) *Black solid circles* are the center positions of polydisperse cylinders produced by jammed packing in a computer simulation. *Blue thin lines* represent the Delaunay tessellation, that leads to the formation of a trivalent network structure shown in *red thick lines*. (**b**) Spatial Fourier spectra (*inset*) and spatial correlation function $C(\Delta r)$ (*main panel*) of the trivalent network structure. (*scale bar*: $2\pi/a$) (**c**) Calculated density of optical states for a trivalent network structure (*blue dashed line*) and an amorphous array of air cylinders (*black solid line*) with the same air filling fraction $f = 0.53$ and dielectric refractive index $n_e = 2.68$. (**d**) Calculated Q factor of the resonant modes in the trivalent network structure as a function of the normalized frequency a/λ. (**e**) and (**f**) are calculated intensity distributions of two modes [*circled* in (**d**)] at the low and high frequency sides of the bandgap. Reprinted with permission from [49], Copyright 2008, Wiley-VCH

a finite-difference time-domain (FDTD) simulation [36]. The boundary condition is periodic, and the supercell contains 2048 vertices. Only TE modes are considered, as the lasing modes in the GaAs membrane are TE polarized due to stronger amplification by QDs. Figure 9.16 (c) displays a significant depletion of DOS in the 2D trivalent network. For comparison, we calculated the DOS for an amorphous array of monodisperse air cylinders in GaAs. This structure was derived from the jammed packing of polydisperse cylinders (from which the network structure was created) by reducing the radii of all cylinders to a constant value. The air filling fraction f is identical to that in the network structure. As seen in Fig. 9.16 (c), the DOS has only a shallow dip in the amorphous array of air cylinders. Hence, the PBG effect is greatly enhanced in the trivalent network structure. This is attributed to the uniform topology of each junction.

Next we calculated the quality factor ($Q \equiv \omega\tau$, ω is the frequency, τ is the lifetime) of the resonant modes in the 2D structure with the finite-element method (using the commercial software Comsol) in 2D. The network has 2048 vertices and open boundary. As shown in Fig. 9.16 (d), there are no guided modes with TE polarization in the frequency range $a/\lambda = 0.32$ and 0.38, as a result of the complete PBG for TE guided modes. The highest-Q modes are located at the BEs. They are tightly confined within the structure, as seen in Fig. 9.16 (e, f). The spatial localization of BE modes reduces light leakage through the boundary of the structure, resulting in high Q factor. This is distinct from the periodic structure whose BE modes are extended. Figure 9.16 (e)/(f) also reveals that the intensity of the BE mode at the low/high frequency side of the PBG is mostly concentrated in the dielectric/air. Thus it can be labeled as the dielectric/air BE mode.

The computer generated patterns of 2D trivalent network were transfered to a GaAs membrane containing InAs quantum dots (QDs). Figure 9.17 (a) is a top-view scanning electron microscope (SEM) image of one pattern with $a = 315$ nm. The lateral dimension of each pattern is 9.7 μm × 9.7 μm. A series of patterns with different a were fabricated. The lasing experimental setup is the same as that in the previous Sect. 9.2.2. We realized lasing in a network structure of $a = 315$ nm with optical excitation of InAs QDs. The emission spectrum consists of a few narrow peaks on top of a broad background [top curve in Fig. 9.18 (a)]. The background originates from the broad-band amplified spontaneous emission, while the narrow peaks correspond to the resonant modes. Figure 9.17 (b) plots the intensity of one emission peak at wavelength $\lambda = 1000$ nm versus the incident pump power P. It displays a threshold behavior. When P exceeds 9.8 μW, the emission intensity increases much more rapidly with P. The full width at half maximum (FWHM) of the peak also decreases dramatically with increasing P and reaches the value of 0.28 nm at $P = 16$ μW. Such behaviors indicate the onset of lasing action. The optical image of the lasing mode, shown in Fig. 9.19 (a), reveals the mode is located in the interior of the pattern. Its lateral size was approximately 2.4 μm, significantly smaller than the pattern size (9.7 μm). With a further increase of pump power, we observed lasing in multiple modes.

We repeated the lasing experiment on different network configurations with the same a. They were generated from different jammed packings of polydisperse cylin-

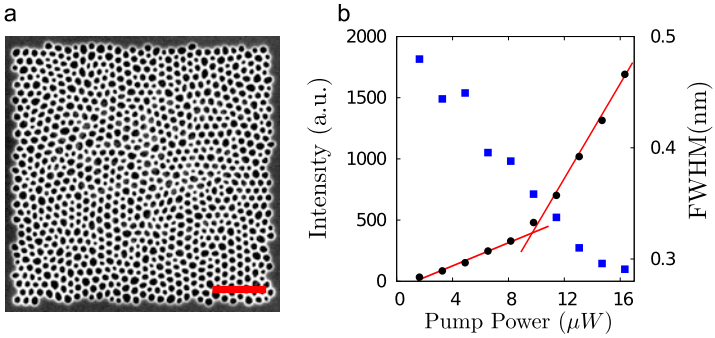

Fig. 9.17 (**a**) A plane-view scanning electron microscope image of the fabricated trivalent network structure in a GaAs membrane with $a = 315$ nm. The *scale bar* is 2 μm. (**b**) Measured intensity (*black circle*) and spectral width (*blue square*) of one emission peak at $\lambda = 1000$ nm as a function of the incident pump power P. Reprinted with permission from [49], Copyright 2008, Wiley-VCH

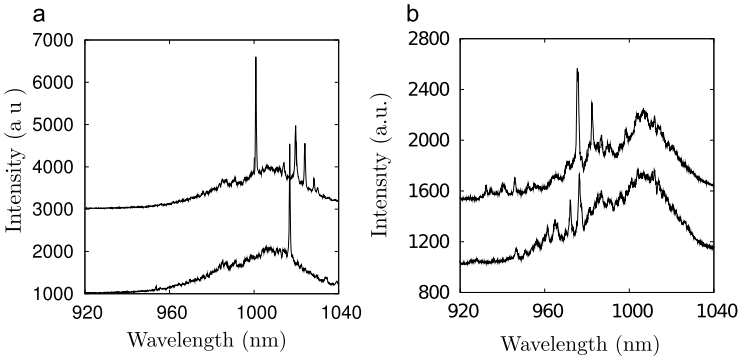

Fig. 9.18 Measured emission spectra for the trivalent network structures of $a = 315$ nm in (**a**), and 275 nm in (**b**). The two spectra in each panel are taken from different configurations. With decreasing a, the lasing modes blue shift. Reprinted with permission from [49], Copyright 2008, Wiley-VCH

ders. Their spatial Fourier spectra and spatial correlation functions are nearly identical, indicating these configurations are statistically equivalent. Lasing was realized in these patterns within the same spectral range, although the frequencies of individual lasing modes varied from pattern to pattern [Fig. 9.18 (a)].

We performed 3D FDTD simulation of the real structures that were extracted from the digitized SEM images. The results illustrated that the lasing modes are located near the dielectric BE of the PBG. The air BE is located at much shorter wavelength $\lambda \simeq 720$ nm. The air BE modes could not lase as they are beyond the gain spectrum of InAs QDs. Although they can be tuned into the gain spectrum by increasing a, the dielectric BE modes are preferred for lasing as they are concentrated in the GaAs and experience more gain from the InAs QDs. We calculated a dielectric BE mode in the 3D FDTD simulation. As shown in Fig. 9.19 (b), the

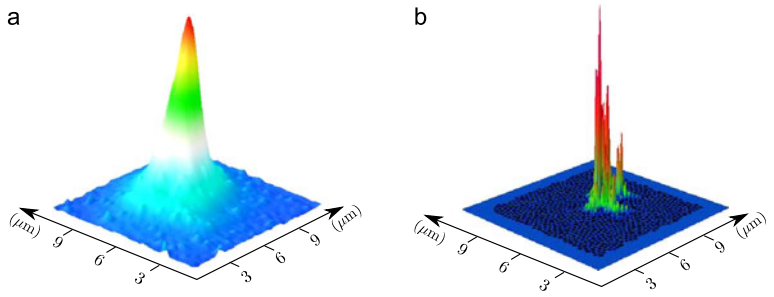

Fig. 9.19 (**a**) Optical image of the lasing mode in Fig. 9.17 (**b**). (**b**) Spatial intensity distribution of the dielectric BE mode calculated in a 3D FDTD simulation of the real structure

mode is spatially localized and has a size is similar to the measured one Fig. 9.19 (a). However, the fine features, e.g., closely-spaced intensity maxima, were smeared out in the optical image due to a finite resolution of our imaging system. The Q factor of this mode is about 6000, which is limited by the out-of-plane leakage of light.

Finally we probed lasing in trivalent network structures of different a. Figure 9.18 (b) displays the emission spectra taken from two configurations of $a =$ 275 nm. Lasing peaks shift to shorter wavelength. This move is consistent with the blue shift of the dielectric BE as a decreases. However, the 3D FDTD calculation predicted that the dielectric BE shift to $\lambda \sim 900$ nm, but the lasing peaks were seen around 975 nm. Although the dielectric BE modes at 900 nm have higher Q, they are far from the peak of gain spectrum and experience much lower gain than the modes at 975 nm. Thus the latter have lower lasing threshold and dominated the lasing spectra.

9.3.2 3D Photonic Network Structures

Although many studies have demonstrated that PBGs can be formed in 2D and 3D PAS with short-range order [10, 14, 16–18, 48, 50], the exact physical mechanism or condition for the PBG formation in PAS is not well understood. Our recent numerical study aims to improve the fundamental understanding of PBG formation in PAS, which would allow researchers to design photonic amorphous materials with optimized and tunable PBGs.

In addition to geometric order, structural topology plays an important role in forming a PBG. For the composite dielectric materials consisting of two components with different refractive indices, there are two cases regarding the topology of the high-index component. (i) Cermet topology: the high-index material consists of isolated inclusions, each of which is completely surrounded by the low-index material. (ii) Network topology: the high-index material is connected and forms a continuous network running through the whole composite. Previous studies of periodic structures have indicated that the cermet topology is more favorable for the

PBG formation of a scalar wave, while the network topology for a vector field [51]. Such conclusions also apply to PAS. For example, in 2D PAS, PBGs for the transverse magnetic (TM) polarization (electric field out of plane) are easily obtained with isolated islands of high-index materials, because the electric field has same polarization direction everywhere and can be regarded as a scalar wave. For the transverse electric (TE) polarization (electric field in plane), the electric field has varying polarization direction and behaves like a vector field, thus it is easier to produce PBGs in connected dielectric networks [52]. It has been proposed that a hybrid structure with a mixture of both topologies can possess a full PBG for both TE and TM polarizations [17].

It is much more difficult to form complete PBGs in 3D structures. Substantial reductions in the density of optical states (DOS) have been demonstrated in PAS composed of randomly packed dielectric spheres of uniform size [14], as a result of evanescent coupling of the Mie resonances of individual spheres. Dielectric network structures, for example, the photonic amorphous diamond (PAD), exhibit much stronger depletion of the DOS [16, 48]. It was conjectured that the tetrahedral bonding configuration in the PAD plays an important role in the formation of isotropic PBG. However, the PAD is constructed from a "continuous-random-network" (CRN) originally developed for modeling of amorphous Si or Ge [53], thus it is difficult to separate the relative contributions of tetrahedral bonding and local geometric order to the PBG formation. Identifying the key parameters that determine when a PBG will form in PAS is important not only for developing novel photonic glasses [54], but also for understanding color generation in nature [24]. Both cermet and network topologies have been found in color-producing PAS of many animal species [27, 28]. It is also conjectured that pseudo PBGs may be formed and responsible for non-iridescent coloration of many PAS [55].

This section presents a detailed numerical study of the DOS and PBGs in 3D PAS. We vary the topology, short-range geometric order, refractive index contrast, and filling fraction to maximize the depletion of DOS and the strength of PBG in the absence of long-range structural order. This study allows us to identify the essential elements for the formation of PBGs in PAS.

Network Generation and Characterization

We first study dielectric composites with the cermet topology—high-index dielectric spheres embedded within a low-index host material (air). We employ a two-stage numerical protocol to generate 'just-touching', jammed sphere packings in a cubic simulation cell with varying positional order [33, 56]. First, liquid states of monodisperse spheres are cooled at fixed packing fraction $\phi = 0.60$ from an initial high temperature T_0 to zero temperature at different rates. In the second step, each zero-temperature configuration is compressed in steps of $\Delta\phi = 10^{-3}$ followed by minimization of the total energy until a static packing with infinitesimal particle overlaps is obtained. By varying the cooling rate, we are able to create static packings with a range of positional order and packing fractions from random close

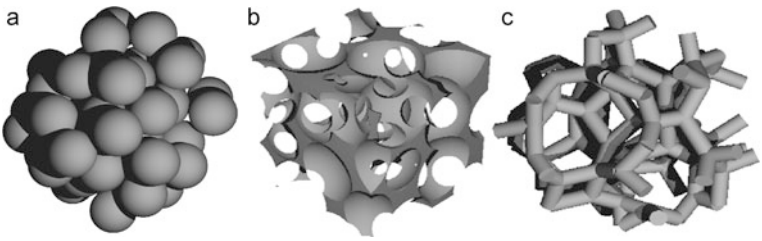

Fig. 9.20 Three examples of photonic amorphous structures: (**a**) jammed packing of dielectric spheres at $\phi = 0.64$, (**b**) inverse structure of (**a**) with air fraction $\gamma = 0.8$, and (**c**) tetrahedral network of dielectric rods with $\gamma = 0.8$ obtained from the Delaunay tessellation of (**a**). Reprinted with permission from [58], Copyright 2008, Wiley-VCH

packing at $\phi = 0.64$ to the face centered cubic (FCC) structure at $\phi = 0.74$. In general, the slowly cooled samples can be compressed to higher packing fractions. Figure 9.20 (a) shows a cluster of 50 spheres from the interior of a jammed sphere packing containing 1000 spheres at $\phi = 0.64$. For comparison, we generate completely disordered configurations by placing spheres randomly in the cubic box with no overlaps at $\phi = 0.35$.

We also generate structures with network topologies, where the high-index dielectric material forms the continuous network, using two methods. For the first method, we invert the cermet structure of jammed dielectric spheres in air. The inverse structure consists of low-index (air) spherical inclusions in a continuous high-index dielectric network. By adjusting the radius R of the spheres (but fixing their positions), we can vary the air fraction γ in the inverse structure. An inverse structure with $\gamma = 0.8$ is shown in Fig. 9.20 (b). At this γ, adjacent air spheres begin to overlap and the dielectric material exhibits an irregular topology.

The second method, which is based on an algorithm described in Refs. [17, 57], produces more uniform network topologies than those from the first method. In this method, a 3D Delaunay tessellation is performed on the sphere centers from the cermet structures. Each tetrahedron of the tessellation has four facets shared with four neighbors. We then calculate the center of mass of each tetrahedron, and connect the centers of mass of nearest neighbors by a dielectric rod. This creates a tetrahedrally connected dielectric network, where each junction (vertex) has four dielectric bonds. All dielectric rods have same radius W, but different lengths d. By changing W, we can vary the air fraction γ. A tetrahedral network with $\gamma = 0.8$ is shown in Fig. 9.20 (c).

We now calculate the density autocorrelation function and spatial Fourier spectra of the cermet and network structures described above. Since the dielectric spheres embedded in air and the corresponding inverted structure possess identical geometrical properties, we focus only on the air spheres and tetrahedral network structures below.

As shown in the inset to Fig. 9.21 (a), the 3D spatial Fourier transform of the tetrahedral network structures displays concentric spherical shells without discrete Bragg peaks, which reflects structural isotropy and a lack of long-range order. The

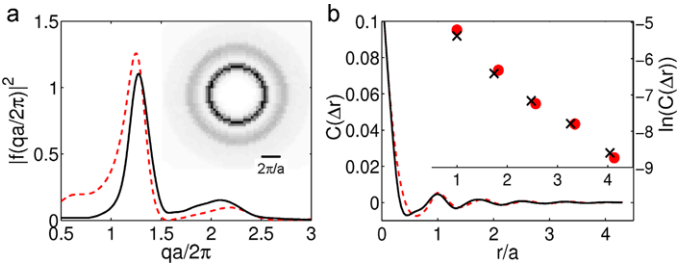

Fig. 9.21 Structural characterization of photonic amorphous structures. (**a**) Angle-averaged power spectra of the spatially Fourier transformed density for jammed sphere packings (*dashed line*) and tetrahedral networks (*solid line*) versus $qa/2\pi$, where q is the spatial frequency and a is the mean spacing between spheres. The *inset* shows a cross-section of the 3D power spectrum for the tetrahedral network. (**b**) Angle-averaged density autocorrelation for the sphere packing and network structures. The *inset* shows the amplitudes of the oscillatory peaks of $C(\Delta r)$ for sphere packings (*circles*) and tetrahedral networks (*crosses*). Reprinted with permission from [58], Copyright 2008, Wiley-VCH

radii of the shells provides the characteristic spatial modulation frequencies of the structures. Similar results are obtained for the tetrahedral networks generated from the jammed sphere packings. The angle-averaged power spectra for both sphere and network structures are plotted in Fig. 9.21 (a). The main peak represents the dominant spatial frequency, and its width is inversely proportional to the average size of ordered domains [19]. The sphere and network structures have similar peak widths, and thus comparable domain sizes.

We also calculated the real-space density autocorrelation function $C(\Delta r)$ averaged over all angles for the sphere and network structures [19]. As shown in Fig. 9.21 (b), both structures display highly damped oscillations of $C(\Delta r)$. The first peak away from $\Delta r = 0$ is located at the average spacing a between nearest neighbors. We find that the amplitudes of the oscillatory peaks decay exponentially [inset to Fig. 9.21 (b)] with a decay length (excluding the first peak) $\xi_r \approx 0.9a$ for the sphere packings and $1.1a$ for the tetrahedral networks. Hence, there are weak spatial correlations and short-range order in these PAS.

DOS of PAS with Cermet and Network Topologies

In this section, we compare the DOS for jammed dielectric spheres in air, the inverse structure, and the tetrahedral networks of dielectric rods using the order-N method [36]. We choose a cubic supercell with size $8.7a$ containing 1000 spheres and refractive indices $n = 3.6$ and 1 for the high- and low-index materials, respectively. We find that the optimal air fraction that yields the largest reduction of the DOS is $\gamma = 0.75$ for the dielectric sphere packings and 0.80 for both the inverse structure and tetrahedral network. The DOS was ensemble-averaged over five distinct configurations at the optimal γ for each topology, and then normalized by the

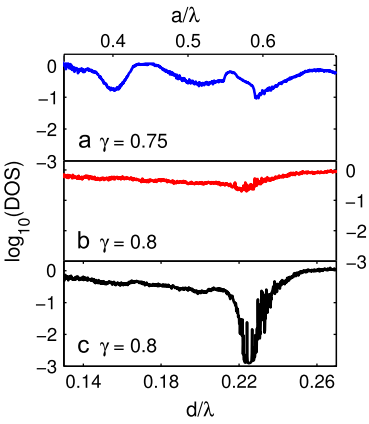

Fig. 9.22 DOS for (**a**) jammed dielectric spheres in air with $\gamma = 0.75$, (**b**) inverted structures with $\gamma = 0.8$, and (**c**) tetrahedral networks with $\gamma = 0.8$. The wavelength λ is normalized by the mean spacing between spheres a (average bond length d) on the *top* (*bottom*) *scale*. Reprinted with permission from [58], Copyright 2008, Wiley-VCH

DOS of a "homogeneous" medium with the same γ. The latter structure is generated by placing cubic dielectric voxels (with lateral dimension $0.043a$, which is much smaller than the wavelength of light λ) randomly in the supercell.

As shown in Fig. 9.22, the maximal DOS reduction occurs in the tetrahedral network structure, which is two orders of magnitude larger than that for the dielectric spheres and inverse structures. For the tetrahedral networks, the PBG is formed at normalized frequency $d/\lambda \approx 0.22$, where d is the average length of dielectric rods and $d/a = 0.39$. The width of the PBG normalized by the gap center frequency is $\sim$5.5 %. The modest reduction in the DOS at $a/\lambda \approx 0.41$ for the dielectric spheres stems from Mie resonances of individual spheres [14]. The uniformity of the dielectric spheres allows the coupling of their Mie resonances, which of the lowest order for isolated dielectric spheres in air occurs at $a/\lambda \approx 0.41$. In contrast, the air sphere structures have only a small reduction of the DOS in the frequency range where the tetrahedral networks show a pronounced PBG, despite the fact that both structures have dielectric network topology and similar degree of spatial correlation. It is clear that the dramatic difference in the DOS cannot be explained by the small differences in spatial correlations.

Our studies of jammed dielectric sphere packings show that uniformity in the size of dielectric spheres leads to strong coupling of Mie resonances that result in a depletion of the DOS. In the inverse structure of air spheres, the basic scattering unit is the dielectric filling between air spheres. For the tetrahedral network structure, the basic scattering unit is centered at each junction where four dielectric rods meet. Note that in the network topology, the adjacent scattering units are connected, in contrast with the cermet topology. To compare the uniformity of local scattering units in dielectric networks, we calculate the average refractive index near the center of each unit. For the tetrahedral network structure, we calculate the mean refractive index $\bar{n}$ within a sphere of radius r whose center coincides with the center of each junction. We then compute the average $\langle \bar{n}(r) \rangle$ and its variance $V(r)$ over all junctions. For the air spheres, the dielectric junction center is set at the center of refractive index distribution within each tetrahedron obtained from the 3D Delaunay

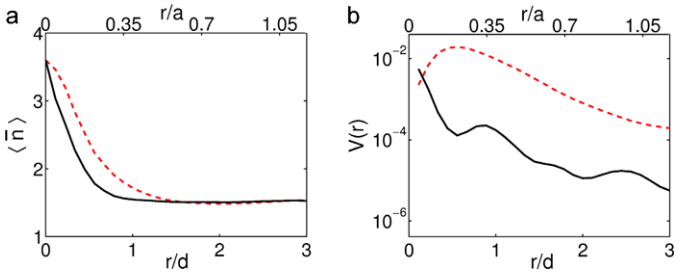

Fig. 9.23 Uniformity of the local scattering environment for the dielectric networks of tetrahedral bonding (*solid line*) and air spheres (*dashed line*). (**a**) Mean index of refraction $\langle \bar{n}(r) \rangle$ and (**b**) variance $V(r)$ within a distance r from the dielectric junction center. r is normalized by the mean spacing of spheres a (average bond length d) on the *top* (*bottom*) *scales*. Reprinted with permission from [58], Copyright 2008, Wiley-VCH

tessellation of the sphere centers. Similarly, we calculate the mean refractive index $\bar{n}$ around each junction center, $\langle \bar{n}(r) \rangle$, and $V(r)$ averaged over all junctions.

In Fig. 9.23 (a) we show that on average the tetrahedral network and air spheres structure have similar distributions of the mean refractive index $\langle \bar{n}(r) \rangle$ around each dielectric junction. In addition, the average refractive index for both networks approaches the same value at large r since the air fraction γ is the same for both structures. However, the variance $V(r)$ of $\bar{n}$ for the two network structures shows marked differences for all r as shown in Fig. 9.23 (b). The tetrahedral network possesses much smaller fluctuations in $\bar{n}$ from one junction to another. Thus, the scattering units are much more uniform for the tetrahedral network than those in the air spheres. The uniformity of local refractive index distribution ensures similar scattering characteristic of individual dielectric junctions and facilitates their coupling which leads to a dramatic depletion of the DOS.

The formation of a PBG in the tetrahedral network structure also depends on the air fraction γ and the refractive index of the dielectric material n. In Fig. 9.24 (a), we show the variation of the PBG for different values of γ while keeping n at 3.6. Reducing the air fraction below 0.8 leads to a decrease in the PBG. A reduction in γ increases the average refractive index of the structure, thus reducing the ratio of the index difference $(n-1)$ to the average refractive index. It leads to a decrease of the overall scattering strength, and a weakening of the PBG. In contrast, if γ is increased to above 0.8, there is an insufficient amount of high-index material to scatter light. Thus, there exists an optimal air fraction γ at which the scattering strength is maximal and the PBG is the largest. The optimal value of γ varies with the refractive index contrast. As shown in Fig. 9.24 (b), as n decreases, the maximal DOS reduction shifts to smaller γ value. In addition, the DOS dip becomes shallower, reflecting the PBG effect is weaker at lower refractive index contrast. While the depth of DOS reduction changes slightly when n varies from 3.6 to 3.2, it drops by nearly two orders of magnitude with a further reduction of n from 3.2 to 2.8. This threshold behavior indicates there is a cut-off value of n for the PBG formation in the tetrahedral network structure.

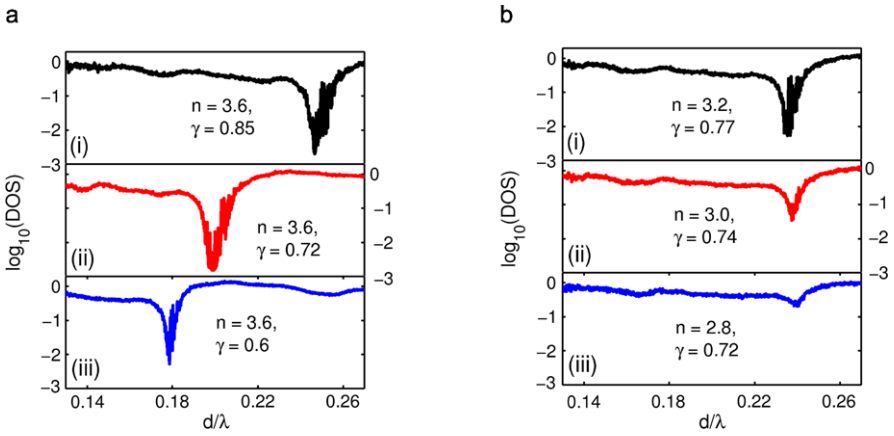

Fig. 9.24 DOS of tetrahedral networks for different values of the air fraction γ and refractive index n. (**a**) $n = 3.6$, (*i*) $\gamma = 0.85$, (*ii*) $\gamma = 0.72$, and (*iii*) $\gamma = 0.6$. (**b**) (*i*) $n = 3.2$, $\gamma = 0.77$, (*ii*) $n = 3.0$, $\gamma = 0.74$ and (*iii*) $n = 2.8$, $\gamma = 0.72$. Reprinted with permission from [58], Copyright 2008, Wiley-VCH

Effects of Short-Range Order

In addition to the factors studied above, short-range positional order and tetrahedral bond order play important roles in the formation of PBGs in PAS. In this section, we focus on the dielectric network of tetrahedral bonding, which yields the largest PBGs, and vary the amount of positional and tetrahedral bond order. In particular, we tune the positional order of the original sphere packings from which the tetrahedral networks are formed. The degree of positional order increases with the volume fraction of spheres ϕ, which varies from 0.35 to 0.69. We label the tetrahedral networks (Fig. 9.25 (a)–(c)) generated from the sphere packings at $\phi = 0.35$, 0.64, and 0.69 as A, B, and C. 2D cross-sections of the 3D spatial Fourier spectra for these structures are presented in Fig. 9.25 (d)–(f). The power spectra of networks A and B consist of concentric shells, but the shell width is notably larger for A. Thus both A and B are isotropic structures, but B possesses more positional order than A. In contrast to A and B, network C features discrete diffraction peaks in the Fourier spectrum, and the structure is no longer isotropic.

In Fig. 9.26, we compare the DOS of the tetrahedral networks A, B, and C, with the refractive index of the dielectric rods set to $n = 3.6$. By adjusting the dielectric rod radius W, we find that the optimal air fraction for all three structures is $\gamma = 0.8$. As expected, network A, with the least positional order, possesses the smallest depletion in the DOS. However, network C with the strongest degree of positional order has a smaller DOS depletion than network B. This result contrasts with recent findings for 2D PAS with air cylinders embedded in dielectric materials that show increasing positional order leads to stronger DOS depletion [19]. To understand these results, we must also compare the uniformity of the local refractive index distribution and the structural topology of the three network structures at

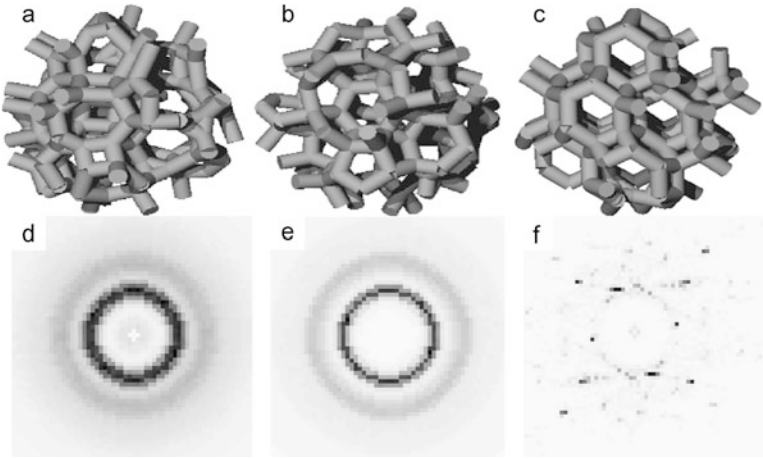

Fig. 9.25 Tetrahedral dielectric networks generated from sphere packings with packing fraction (**a**) $\phi = 0.35$, (**b**) 0.64, and (**c**) 0.69. 2D cross-sections of the 3D spatial Fourier spectra of the corresponding tetrahedral networks are shown in (**d**), (**e**), and (**f**). Reprinted with permission from [58], Copyright 2008, Wiley-VCH

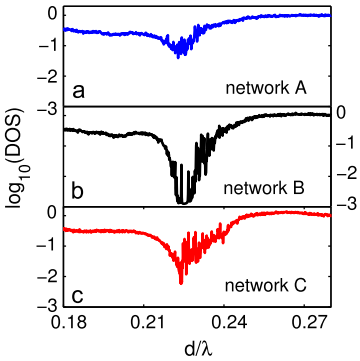

Fig. 9.26 The DOS for three tetrahedral dielectric networks (**a**) A, (**b**) B, and (**c**) C with positional order increasing from A to C. Reprinted with permission from [58], Copyright 2008, Wiley-VCH

fixed radius W of the dielectric rods. We find that networks B and C have comparable fluctuations in $\bar{n}$ over all the junctions. Thus, local uniformity does not explain the difference in the depletion of the DOS for networks B and C.

To investigate the effects of local topology on the depletion of the DOS, we compute the tetrahedral order parameter [17, 48]

$$\zeta = 1 - \frac{3}{8}\sum_{j=1}^{3}\sum_{k=j+1}^{4}\left(\cos\psi_{jk} + \frac{1}{3}\right)^2, \tag{9.10}$$

where ψ_{jk} is the angle between two dielectric rods joined at a junction in the tetrahedral network [59]. For a periodic diamond network, $\psi_{jk} = 109.5°$, $\cos(\psi_{jk}) = -1/3$ for all j and k, and thus $\zeta = 1$ at each junction. If the dielectric rods are ran-

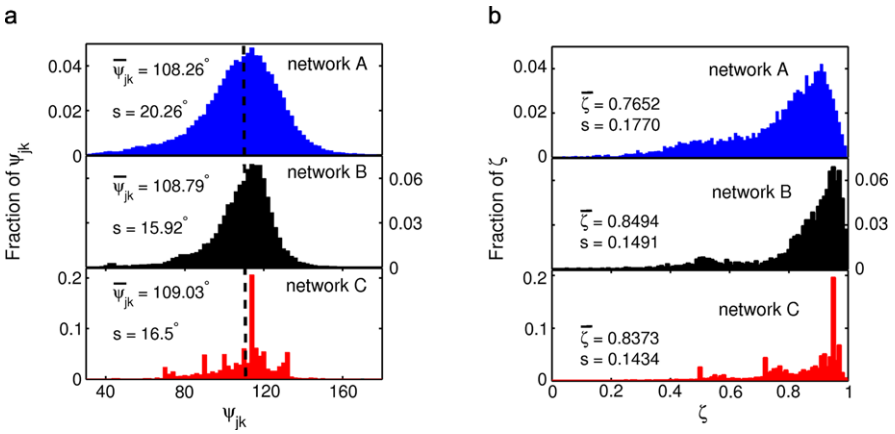

Fig. 9.27 Characterization of the local topology for networks A, B and C. (**a**) The distribution of angles ψ_{jk} between dielectric rods j and k at each tetrahedral junction. The *vertical dashed line* indicates the angle for the periodic diamond structure, $\psi_{jk} = 109.5°$. (**b**) Distribution of the tetrahedral order parameters ζ at each junction. The average $\bar{\psi}_{jk}$ and $\bar{\zeta}$ and standard deviations s_ψ and s_ζ are also provided. Reprinted with permission from [58], Copyright 2008, Wiley-VCH

domly orientated, $\langle \zeta \rangle = 0$. In Fig. 9.27, we plot the distributions of ψ_{jk} and ζ for the A, B, and C networks, and provide the mean values ($\bar{\psi}_{jk}$ or $\bar{\zeta}$), and standard deviations s_ψ and s_ζ.

Network A possesses the widest distributions for both ψ_{jk} and ζ, which indicates that the local topology varies significantly from one junction to another and the bond angles within each junction are not uniform. The distributions of ψ_{jk} and ζ are narrower for network B, and are peaked at $\psi_{jk} = 114°$ and $\zeta = 0.95$, which indicates that most of the junctions have a similar topology to that in a diamond lattice. In contrast, network C displays multi-modal distributions for ψ_{jk} and ζ. For example, the ζ distribution possesses peaks at $\zeta = 0.95, 0.72$, and 0.5. The first peak reveals that there are many junctions with strong tetrahedral order, while the second and third peaks reflect the existence of many "defect" junctions with low ζ. Such defect junctions are likely located at domain boundaries, and introduce irregularity in the local configuration of scattering units. Figures 9.26 and 9.27 show that photonic amorphous networks with strong tetrahedral order and few defect junctions have broad PBGs.

9.4 Conclusion

In our numerical study on the density of optical states (DOS) in 2D photonic structures with short-range positional order, we observe a transition from polycrystalline to amorphous photonic systems. In polycrystals, photonic band gaps (PBGs) are formed within individual domains, which leads to a depletion of the DOS similar to that in periodic structures. In amorphous photonic media, the domain sizes are too

small to form PBGs, thus the depletion of the DOS is weakened significantly. The critical domain size that separates the polycrystalline and amorphous regimes is determined by the attenuation length of Bragg scattering, which depends not only on the degree of positional order but also the refractive index contrast of the photonic material. Even with relatively low refractive index contrast, we find that modest short-range positional order in photonic structures enhances light confinement via collective scattering and interference.

Experimentally we have demonstrated lasing in photonic polycrystals and amorphous structures. 2D arrays of air holes were fabricated in a free-standing GaAs membrane, and the average size of ordered domains was gradually varied. InAs QDs embedded in the GaAs membrane provide gain under optical pumping. In a photonic polycrystal, defect modes at the center frequency of PBG are tightly confined in-plane, causing strong light leakage out of the plane. The lasing modes shift away from the PBG center to reduce the out-of-plane leakage. In a photonic amorphous structure, the depletion of DOS is significantly weakened, and the lasing modes have less in-plane confinement. Nevertheless, the short-range structural order improves optical confinement and enhances the Q factor at certain frequency. Consequently, lasing becomes the most efficient, i.e., the laser emission becomes the strongest, at such frequency. The optimal lasing frequency can be tuned by the structure factor. The photonic polycrystal laser and amorphous laser are in between the photonic crystal laser and random laser. Our study demonstrates that lasing can be manipulated by varying the short-range order of the nanostructures.

In addition, we compare the DOS in 3D photonic amorphous structures with cermet and network topologies. We find that interconnected networks of high-index material with uniform dielectric junctions and tetrahedral bonding give rise to large isotropic PBGs. Further, reduced fluctuations in the refractive index around each junction and strong tetrahedral order for the angles between the dielectric rods that form the junctions enhance isotropic PBGs. High refractive index contrast and a low fraction of high-index material are also important to PBG formation. We have thus identified several parameters that can be tuned to create broad isotropic PBGs in photonic amorphous structures in the absence of long-range structural order.

We also fabricate 2D trivalent network structures with short-range order in a free-standing GaAs membrane. Such structures display wide isotropic photonic bandgaps. We have realized lasing in the dielectric bandedge modes with optical pumping. The bandedge modes are spatially localized, different from the extended bandedge modes in photonic crystals. By varying the characteristic length scale of the network structure, we can tune the lasing frequency within the gain spectrum of InAs quantum dots.

The future work includes fabrication of 3D photonic network structures, which is more difficult than fabricating 2D structures. Since such structures have only short-range order, they may be fabricated by self-assembly, which is much easier than the fabrication of 3D periodic structures. In fact, 3D photonic network structures have already been produced routinely in nature, and our preliminary studies suggest they are formed by phase separation, e.g., spinodal decomposition [27]. We can mimic nature to make photonic amorphous structures in mass quantity at room temperature [60]. Furthermore we can outperform the natural structures by using inorganic

materials with large refractive index contrast to enhance the interaction with light, or incorporating active materials with gain or nonlinearity to achieve new functionalities.

Acknowledgements We thank our co-workers who have contributed to the studies presented in this chapter. Dr. Jin-Kyu Yang and Seng-Fatt Liew performed experimental and numerical studies on PBG and lasing in photonic nanostructures with short-range order. Prof. Corey O'Hern and Carl Schreck developed the numerical methods to generate the amorphous nanostructures. Prof. Glenn Solomon grew the semiconductor samples by molecular beam epitaxy, Dr. Michael Rooks worked with us in fabricating the nanostructures with the electron-beam lithography, and Dr. Mikhail Guy assisted us in the computer simulation. We acknowledge Professors Eric Dufresne, Richard Prum, A. Douglas Stone, Simon Mochrie, and Dr. Vinodkumar Saranathan for many stimulating discussions and the collaborative studies on coloration of photonic amorphous structures in nature. Our research program has been sponsored by the National Science Foundation, and the Materials Research and Engineering Center at Yale University.

References

1. S. Noda, T. Baba (eds.), *Roadmap on Photonic Crystals* (Kluwer Academic, Dordrecht, 2003)
2. M. Meier, A. Mekis, A. Dodabalapur, A. Timko, R.E. Slusher, J.D. Joannopoulos, O. Nalamasu, Laser action from two-dimensional distributed feedback in photonic crystals. Appl. Phys. Lett. **74**(1), 7–9 (1999)
3. O. Painter, R.K. Lee, A. Scherer, A. Yariv, J.D. O'Brien, P.D. Dapkus, I. Kim, Two-dimensional photonic band-gap defect mode laser. Science **284**(5421), 1819–1821 (1999)
4. H.-G. Park, S.-H. Kim, S.-H. Kwon, Y.-G. Ju, J.-K. Yang, J.-H. Baek, S.-B. Kim, Y.-H. Lee, Electrically driven single-cell photonic crystal laser. Science **305**(5689), 1444–1447 (2004)
5. M. Notomi, H. Suzuki, T. Tamamura, K. Edagawa, Lasing action due to the two-dimensional quasiperiodicity of photonic quasicrystals with a penrose lattice. Phys. Rev. Lett. **92**(12), 123906 (2004)
6. K. Nozaki, T. Baba, Quasiperiodic photonic crystal microcavity lasers. Appl. Phys. Lett. **84**(24), 4875–4877 (2004)
7. S.-K. Kim, J.-H. Lee, S.-H. Kim, I.-K. Hwang, Y.-H. Lee, S.-B. Kim, Photonic quasicrystal single-cell cavity mode. Appl. Phys. Lett. **86**(3), 031101 (2005)
8. K. Nozaki, T. Baba, Lasing characteristics of 12-fold symmetric quasi-periodic photonic crystal slab nanolasers. Jpn. J. Appl. Phys. **45**(8A), 6087–6090 (2006)
9. X. Xu, H. Chen, D. Zhang, Enhancement of stimulated emission in 12-fold symmetric quasicrystals. Appl. Phys. B **89**, 29–34 (2007)
10. C. Jin, X. Meng, B. Cheng, Z. Li, D. Zhang, Photonic gap in amorphous photonic materials. Phys. Rev. B **63**(19), 195107 (2001)
11. J. Ballato, J. Dimaio, A. James, E. Gulliver, Photonic band engineering through tailored microstructural order. Appl. Phys. Lett. **75**(11), 1497–1499 (1999)
12. C. Rockstuhl, U. Peschel, F. Lederer, Correlation between single-cylinder properties and bandgap formation in photonic structures. Opt. Lett. **31**(11), 1741–1743 (2006)
13. Y. Wang, S. Jian, Band-gap engineering of amorphous photonic materials. Phys. Lett. A **352**(6), 550–553 (2006)
14. C. Rockstuhl, F. Lederer, Suppression of the local density of states in a medium made of randomly arranged dielectric spheres. Phys. Rev. B **79**(13), 132202 (2009)
15. P.D. García, R. Sapienza, Á. Blanco, C. López, Photonic glass: a novel random material for light. Adv. Mater. **19**(18), 2597–2602 (2007)
16. K. Edagawa, S. Kanoko, M. Notomi, Photonic amorphous diamond structure with a 3D photonic band gap. Phys. Rev. Lett. **100**(1), 013901 (2008)

17. M. Florescu, S. Torquato, P.J. Steinhardt, Designer disordered materials with large, complete photonic band gaps. Proc. Natl. Acad. Sci. **106**(49), 20658–20663 (2009)
18. M. Rechtsman, A. Szameit, F. Dreisow, M. Heinrich, R. Keil, S. Nolte, M. Segev, Amorphous photonic lattices: band gaps, effective mass, and suppressed transport. Phys. Rev. Lett. **106**, 193904 (2011)
19. J.-K. Yang, C. Schreck, H. Noh, S.-F. Liew, M.I. Guy, C.S. O'Hern, H. Cao, Photonic-band-gap effects in two-dimensional polycrystalline and amorphous structures. Phys. Rev. A **82**(5), 053838 (2010)
20. H. Noh, J.-K. Yang, S.F. Liew, M.J. Rooks, G.S. Solomon, H. Cao, Control of lasing in biomimetic structures with short-range order. Phys. Rev. Lett. **106**, 183901 (2011)
21. J.-K. Yang, H. Noh, S.F. Liew, M.J. Rooks, G.S. Solomon, H. Cao, Lasing modes in polycrystalline and amorphous photonic structures. Phys. Rev. A **84**, 033820 (2011)
22. P. Vukusic, R.J. Sambles, Photonic structures in biology. Nature **424**(6950), 852–855 (2003)
23. S. Kinoshita, S. Yoshioka, Structural colors in nature: the role of regularity and irregularity in the structure. ChemPhysChem **6**(8), 1442–1459 (2005)
24. R.O. Prum, Anatomy, physics, and evolution of structural colors, in *Bird Coloration*, vol. 1 (Harvard University Press, Cambridge, 2006), pp. 295–353
25. P. Simonis, J.P. Vigneron, Structural color produced by a three-dimensional photonic polycrystal in the scales of a longhorn beetle: Pseudomyagrus waterhousei (coleoptera: Cerambicidae). Phys. Rev. E **83**(1), 011908 (2011)
26. K. Kertész, Z. Bálint, Z. Vértesy, G.I. Márk, V. Lousse, J.P. Vigneron, M. Rassart, L.P. Biró, Gleaming and dull surface textures from photonic-crystal-type nanostructures in the butterfly Cyanophrys remus. Phys. Rev. E **74**, 021922 (2006)
27. E.R. Dufresne, H. Noh, V. Saranathan, S.G.J. Mochrie, H. Cao, R.O. Prum, Self-assembly of amorphous biophotonic nanostructures by phase separation. Soft Matter **5**(9), 1792 (2009)
28. H. Noh, S.F. Liew, V. Saranathan, S.G.J. Mochrie, R.O. Prum, E.R. Dufresne, H. Cao, How noniridescent colors are generated by quasi-ordered structures of bird feathers. Adv. Mater. **22**(26–27), 2871–2880 (2010)
29. L.F. Rojas-Ochoa, J.M. Mendez-Alcaraz, J.J. Sáenz, P. Schurtenberger, F. Scheffold, Photonic properties of strongly correlated colloidal liquids. Phys. Rev. Lett. **93**(7), 073903 (2004)
30. A. Derode, V. Mamou, A. Tourin, Influence of correlations between scatterers on the attenuation of the coherent wave in a random medium. Phys. Rev. E **74**, 036606 (2006)
31. M. Reufer, L.F. Rojas-Ochoa, S. Eiden, J.J. Sáenz, F. Scheffold, Transport of light in amorphous photonic materials. Appl. Phys. Lett. **91**(17), 171904 (2007)
32. Y. Takeoka, M. Honda, T. Seki, M. Ishii, H. Nakamura, Structural colored liquid membrane without angle dependence. ACS Appl. Mater. Interfaces **1**(5), 982–986 (2009)
33. G.-J. Gao, J. Bławzdziewicz, C.S. O'Hern, Frequency distribution of mechanically stable disk packings. Phys. Rev. E **74**, 061304 (2006)
34. J.Q. Broughton, G.H. Gilmer, J.D. Weeks, Molecular-dynamics study of melting in two dimensions. inverse-twelfth-power interaction. Phys. Rev. B **25**, 4651–4669 (1982)
35. P.J. Steinhardt, D.R. Nelson, M. Ronchetti, Bond-orientational order in liquids and glasses. Phys. Rev. B **28**, 784–805 (1983)
36. C.T. Chan, Q.L. Yu, K.M. Ho, Order-N spectral method for electromagnetic waves. Phys. Rev. B **51**, 16635–16642 (1995)
37. E. Lidorikis, M.M. Sigalas, E.N. Economou, C.M. Soukoulis, Gap deformation and classical wave localization in disordered two-dimensional photonic-band-gap materials. Phys. Rev. B **61**, 13458–13464 (2000)
38. G. Pompe, T. Rappen, M. Wehner, F. Knop, M. Wegener, Transient response of a short-cavity semiconductor laser. Phys. Status Solidi (b) **188**(1), 175–180 (1995)
39. F. Jahnke, S.W. Koch, Many-body theory for semiconductor microcavity lasers. Phys. Rev. A **52**, 1712–1727 (1995)
40. C. Vanneste, P. Sebbah, Complexity of two-dimensional quasimodes at the transition from weak scattering to Anderson localization. Phys. Rev. A **79**, 041802 (2009)

41. J.B. Pendry, Quasi-extended electron states in strongly disordered systems. J. Phys. C **20**(5), 733 (1987)
42. S.G. Johnson, J.D. Joannopoulos, Block-iterative frequency-domain methods for maxwell's equations in a planewave basis. Opt. Express **8**(3), 173–190 (2001)
43. X. Wu, J. Andreasen, H. Cao, A. Yamilov, Effect of local pumping on random laser modes in one dimension. J. Opt. Soc. Am. B **24**(10), A26–A33 (2007)
44. J. Andreasen, H. Cao, Creation of new lasing modes with spatially nonuniform gain. Opt. Lett. **34**(22), 3586–3588 (2009)
45. J. Andreasen, C. Vanneste, L. Ge, H. Cao, Effects of spatially nonuniform gain on lasing modes in weakly scattering random systems. Phys. Rev. A **81**, 043818 (2010)
46. S.F. Liew, J. Forster, H. Noh, C.F. Schreck, V. Saranathan, X. Lu, L. Yang, R.O. Prum, C.S. O'Hern, E.R. Dufresne, H. Cao, Short-range order and near-field effects on optical scattering and structural coloration. Opt. Express **19**(9), 8208–8217 (2011)
47. S. Fraden, G. Maret, Multiple light scattering from concentrated, interacting suspensions. Phys. Rev. Lett. **65**(4), 512–515 (1990)
48. S. Imagawa, K. Edagawa, K. Morita, T. Niino, Y. Kagawa, M. Notomi, Photonic band-gap formation, light diffusion, and localization in photonic amorphous diamond structures. Phys. Rev. B **82**(11), 115116 (2010)
49. H. Noh, J.-K. Yang, S.F. Liew, M.J. Rooks, G.S. Solomon, H. Cao, Photonic network laser. Opt. Lett. **36**(18), 3560–3562 (2011)
50. H. Miyazaki, M. Hase, H.T. Miyazaki, Y. Kurokawa, N. Shinya, Photonic material for designing arbitrarily shaped waveguides in two dimensions. Phys. Rev. B **67**, 235109 (2003)
51. E.N. Economou, M.M. Sigalas, Classical wave propagation in periodic structures: cermet versus network topology. Phys. Rev. B **48**, 13434–13438 (1993)
52. R.D. Meade, A.M. Rappe, K.D. Brommer, J.D. Joannopoulos, Nature of the photonic band gap: some insights from a field analysis. J. Opt. Soc. Am. B **10**(2), 328–332 (1993)
53. G.T. Barkema, N. Mousseau, High-quality continuous random networks. Phys. Rev. B **62**, 4985–4990 (2000)
54. P.D. García, R. Sapienza, C. López, Photonic glasses: a step beyond white paint. Adv. Mater. **22**(1), 12–19 (2010)
55. B.Q. Dong, X.H. Liu, T.R. Zhan, L.P. Jiang, H.W. Yin, F. Liu, J. Zi, Structural coloration and photonic pseudogap in natural random close-packing photonic structures. Opt. Express **18**(14), 14430–14438 (2010)
56. C.S. O'Hern, L.E. Silbert, A.J. Liu, S.R. Nagel, Jamming at zero temperature and zero applied stress: the epitome of disorder. Phys. Rev. E **68**, 011306 (2003)
57. O. Sigmund, K. Hougaard, Geometric properties of optimal photonic crystals. Phys. Rev. Lett. **100**, 153904 (2008)
58. S.F. Liew, J.-K. Yang, H. Noh, C.F. Schreck, E.R. Dufresne, C.S. O'Hern, H. Cao, Photonic band gaps in three-dimensional network structures with short-range order. Phys. Rev. A **84**, 063818 (2011)
59. P.-L. Chau, A.J. Hardwick, A new order parameter for tetrahedral configurations. Mol. Phys. **93**(3), 511–518 (1998)
60. J.D. Forster, H. Noh, S.F. Liew, V. Saranathan, C.F. Schreck, L. Yang, J.-G. Park, R.O. Prum, S.G.J. Mochrie, C.S. O'Hern, H. Cao, E.R. Dufresne, Biomimetic isotropic nanostructures for structural coloration. Adv. Mater. **22**(26–27), 2939–2944 (2010)